LAWRENCE
LIVERMORE
NATIONAL
LABORATORY

UCRL-JRNL-232511

Explosive hydrogen burning during type I X-ray bursts

J. L. Fisker, H. Schatz, F.-K. Thielemann

July 5, 2007

Astrophysical Journal Supplement Series

Updated October 14, 2003

Explosive hydrogen burning during type I X-ray bursts[1]

Jacob Lund Fisker[1]
Department of Physics and Joint Institute for Nuclear Astrophysics, University of Notre Dame, Notre Dame, IN 46566, USA
jfisker@nd.edu

Hendrik Schatz
Department of Physics and Astronomy and National Superconducting Cyclotron Laboratory and Joint Institute for Nuclear Astrophysics, Michigan State University, East Lansing, MI 48824-2320
schatz@nscl.msu.edu

Friedrich-Karl Thielemann
Department of Physics and Astronomy, University of Basel, Klingelbergstrasse 82, 4056 Basel, Switzerland
F-K.Thielemann@unibas.ch

ABSTRACT

Explosive hydrogen burning in type I X-ray bursts (XRBs) is driven by charged particle reactions creating isotopes with masses up to $A \sim 100$. Since charged particle reactions in a stellar environment are very temperature sensitive, we use a realistic time-dependent general relativistic and self-consistent model of type I X-ray bursts to provide accurate values of the burst temperatures and densities. This allows a detailed and accurate time-dependent identification of the reaction flow from the surface layers through the convective region and the ignition region to the neutron star ocean. Using this, we determine the relative importance of specific nuclear reactions in the X-ray burst.

Subject headings: X-rays: bursts — nuclear reactions, nucleosynthesis, abundances — stars: neutron

1. Introduction

Type I X-ray Bursts (XRBs) (see Bildsten (1998); Strohmayer & Bildsten (2006) for reviews) were first explained by Woosley & Taam (1976) who associated the XRBs with thermonuclear runaways on the surface of neutron stars that accrete a mixture of hydrogen and helium from a semi-detached low mass companion star (Joss 1977). In Woosley & Taam's *thermonuclear flash model* the accreted matter is heated by the impact on the neutron star surface to $1 - 2 \times 10^8$ K, which leads to full ionization. This heating explains the persistently observed X-ray emissions. The accreted matter then undergoes gradual compression as new matter continuously piles on top of it. Under these atmospheric conditions the electrons are degenerate, but the nucleons are not. Therefore the matter is subject to a thin-shell instability that triggers a thermonuclear runaway (Hansen & van Horn 1975). For accretion rates below roughly one Eddington ($\dot{M}^0 = 1.12 \times 10^{18} \mathrm{g\,s^{-1}}$), the bottom layer of the newly accreted matter becomes unstable after a few hours/days and burns explosively giving rise to a burst of X-rays as the atmosphere is heated to 1-1.5 GK. The sudden release of nuclear binding energy heats the atmosphere rapidly

[1]Now at N-division, Lawrence Livermore National Laboratory, P.O. Box 808, Livermore, CA 94551

[1]UCRL-JRNL-232511

and increases the luminosity within a few seconds to its peak value. The luminosity then decreases exponentially as the atmosphere cools producing the observational features of a type I X-ray burst (Joss 1978; Taam 1980). These bursts are the most common thermonuclear explosions in the universe. The fact that the bursts do not destroy the system but can be observed repeatedly makes LMXBs useful to study the behavior of matter under extreme temperature and density conditions.

X-ray bursts have been explored theoretically by Hanawa et al. (1983); Fujimoto et al. (1987); Koike et al. (1999) and stable burning has been explored by Schatz et al. (1999) using relatively simple one-zone models to estimate the burning conditions e.g. a set of $(\rho, T, \vec{X})$, where ρ is the density, T is the temperature, and $\vec{X}$ is a composition array describing the fractional concentration of each isotope. On the other hand more realistic 1 dimensional multi-zone models have been constructed by many groups (Joss 1978; Taam & Picklum 1979; Hanawa et al. 1983; Wallace et al. 1982; Ayasli & Joss 1982) but they suffered from relatively simple nuclear reaction networks. Only recently models have successfully included both aspects (Woosley et al. 2004; Fisker et al. 2004, 2006).

The relevant types of reaction sequences in XRBs have been discussed by Wallace & Woosley (1981); Champagne & Wiescher (1992); van Wormer et al. (1994); Herndl et al. (1995); Schatz et al. (1998); Schatz & Rehm (2006). Important are (p,γ)-, (α,γ)-, (p,α)-reaction rates as well as β-decay rates between the valley of stability and the proton drip line. Reaction rates must be known up to the end-point of the *rp*-process (Schatz et al. 2001a).

In the past serveral attempts have been made to identify critical reaction rates in X-ray bursts. It is, however, not possible to directly test the astronomical number of possible perturbations of the thousands of participating reaction rates. Woosley et al. (2004) changed groups of decay rates and narrowed the rates down to several important candidates. Fisker (2004); Fisker et al. (2004, 2006) relied on "inspired guesses" and found individual important rates. Recently, Amthor et al. (2006) used a one-zone model and individually varied a large number of reaction rates with the intent of verifying "one-zone"-candidates with a multi-zone model. Using Monte Carlo methods, Roberts et al. (2006) varied random groups of reaction rates and similarly identified the most significant candidates for later verification with multi-zone models.

In this paper, we use such a full 1D X-ray burst model with a complete nuclear reaction network to answer one of the fundamental questions in this field: what are the nuclear reactions that power X-ray bursts? While previous studies have used simplified models to delineate basic types of reaction sequences we can now go the next step and describe the actual nuclear reaction sequences that occur as a function of time and depth during a typical X-ray burst. Because temperature, density, and initial composition vary greatly as a function of depth there is no single reaction flow, but a range of very different sequences that influence each other. Identifying the nuclear reactions that take place in X-ray bursts is a prerequisite for understanding X-ray burst light curve features in terms of the underlying nuclear physics and for determining the nuclear physics uncertainties in X-ray burst model predictions of light curves and other observables. It is also essential to guide experimental and theoretical efforts to address these uncertainties in the future.

Cross sections have typically been predicted by global models, which in most cases have been fitted to stable nuclei to be then extrapolated to proton-rich isotopes. In many cases cross sections have also been predicted by nuclear shell model calculations. However, with upgrades of existing experimental facilities and the construction of new facilities many of these reactions are now within reach of experiments (Käppeler et al. 1998; Wiescher 2001; Wiescher & Schatz 2001; Schatz 2002). With a better understanding of the nuclear physics it will also become possible to address potential issues beyond the 1D approximation, such as the interplay of lateral flame propagation and nuclear energy release timescales that can affect the modeling of burst rise times.

2. The 1D multi-zone computational burst model

In this paper we compute and describe one XRB model using the parameters $M = 1.4M_{\odot}$, $R = 11$km corresponding to a redshift of $1 + z = (1 - 2GM/Rc^2)^{-1/2} = 1.27$. We use a global

accretion rate of $\dot{M}^{\infty} = 0.88 \cdot 10^{17}$g/s as observed from infinity which is equivalent to $\dot{M}^{0} = (1+z)\dot{M}^{\infty} = 1.12 \cdot 10^{17}$g/s (0.1 Eddington) in the local proper frame at the surface. The persistent accretion luminosity for these parameters is $L_p^{\infty} = (1+z)^{-2}L^0 = z(1+z)^{-1}\dot{M}^{\infty}c^2 = 1.68 \times 10^{37}\mathrm{ergs\,s^{-1}}$ (Ayasli & Joss 1982).

This choice yields a H/He-ignited XRB corresponding to case (1) of Fujimoto et al. (1981) where the observational data depends more on the *rp*-process than is the case for a pure He-ignited XRB (case (2) of Fujimoto et al. (1981)). Our model is therefore comparable to the Newtonian accretion rate of Schatz et al. (2001a,b) and model *zM* of Woosley et al. (2004) which used $\dot{M} = 1.1 \cdot 10^{17}\,\mathrm{g\,s^{-1}}$.

The model is calculated using a general relativistic type I X-ray burst simulation code that is described in more detail in Fisker et al. (2006). The code couples the general relativistic hydrodynamics code, `AGILE` (Liebendörfer et al. 2002), which solves the general relativistic equations in a spherically symmetric geometry on a comoving grid, with the nuclear reaction network solver of Hix & Thielemann (1999). The code includes radiative, conductive, and convective heat transport as described in Thorne (1977) and uses an arbitrarily relativistic and arbitrarily degenerate equation of state. We calculate the radiative opacities due to Thomson scattering and free-free absorption using the analytic formulations of Schatz et al. (1999). We use the same conductivity formulations for electron scattering on electrons, ions, phonons, and impurities as Brown (2000).

The computational domain encompasses a rest mass of 5.9×10^{22} g covering about 7 pressure scale heights. It is discretized into 129 log-ratioed grid zones with a column density[2] ranging from $y = 1.2 \times 10^{6}$ g cm^{-2} ($P = 5 \times 10^{20}\mathrm{ergs\,cm^{-3}}$) to $y = 3.9 \times 10^{9}$ g cm^{-2} ($P = 7.5 \times 10^{23}\mathrm{ergs\,cm^{-3}}$). This is sufficient to simulate all the nuclear reactions associated with the burst. At the top of the computational domain less than 1.5% of the hydrogen and helium is processed into heavier materials during the burst. Extending the computational domain further upwards by including more pressure scale heights would therefore make little difference in the nuclear processing. At the bottom of the computational domain, the ashes are fully processed by thermonuclear reactions and the average mass changes less than 0.1% over a burst. Pycnonuclear reactions and electron captures, which have characteristic reaction timescales several orders of magnitude larger than the time scale of a burst are included in the boundary condition. The computational domain is bounded by a realistic core boundary interface (Brown 2003, 2004) that emits 0.11 MeV/nucleon from the electron captures and pycnonuclear reaction in the ocean and crust, and a relativistically corrected grey atmosphere (Thorne 1977; Weiss et al. 2004), which is integrated numerically out to $P_{surf} = 10^{18}\mathrm{ergs\,cm^{-3}}$ using a 4th order Runge-Kutta method for greater accuracy (Fisker et al. 2006).

The rp-process is naturally limited once it reaches the $A \sim 104$ region because neutron deficient nuclei in this mass range become α-unbound. This terminates the reaction flow via (γ,α) reactions and forms a SnSbTe cycle (Schatz et al. 2001a). This determines the maximum network size that is needed, unless the alpha unbound nuclei can be circumvented in multiple proton exposures. Schatz et al. (2001a) demonstrated that the $A \sim 104$ endpoint can be reached if burst peak temperatures and hydrogen concentration at ignition are high. However, Woosley et al. (2004) showed, that these ignition conditions are only fulfilled for the first burst after the start of accretion on a pure ^{56}Fe atmosphere. Compositional inertia effects (Taam 1993) for subsequent bursts significantly reduce peak temperature and the amount of hydrogen at ignition as ignition occurs at a lower pressure and depth thus limiting the rp-process to $A \lesssim 64$ and producing only a small fraction of heavier isotopes.

The nuclear reaction network used in this work employs 304 isotopes (see table [1]). All the connecting particle reactions are taken from the REACLIB (see Sakharuk et al. (2006)). These reaction rates have also been used in Weinberg et al. (2006). The network includes all isotopes between the valley of stability and the proton drip line up to ^{64}Ge. Here isotopes with β^+-half lives > 1 day are considered "stable" on the timescale of the burst in-

[2] The relativistic column density is mass of a column above an area: $y \equiv \int_{R-r}^{R} \rho \frac{dr}{\Gamma}$ where $\Gamma = \sqrt{1 - 2GM/Rc^2}$, so $P \simeq gy$, where R is the neutron star radius, M is the neutron star mass, ρ is the density, P is the pressure, and $g = GM/\Gamma R^2$ is the surface acceleration of gravity.

Z	A	Z	A	Z	A
n	1	Ar	31–38	Kr	69–74
H	1–3	K	35–39	Rb	73–77
He	3,4	Ca	36–44	Sr	74–78
Li	7	Sc	39–45	Y	77–82
Be	7,8	Ti	40–47	Zr	78–83
B	8,11	V	43–49	Nb	81–85
C	9,11,12	Cr	44–52	Mo	82–86
N	12–15	Mn	47–53	Tc	85–88
O	13–18	Fe	48–56	Ru	86–91
F	17–19	Co	51–57	Rh	89–93
Ne	18–21	Ni	52–62	Pd	90–94
Na	20–23	Cu	54–63	Ag	94–98
Mg	21–25	Zn	55–66	Cd	95–99
Al	22–27	Ga	59–67	In	98–104
Si	24–30	Ge	60–68	Sn	99–105
P	26–31	As	64–69	Sb	106
S	27–34	Se	65–72	Te	107
Cl	30–35	Br	68–73		

Table 1: The table shows the list of isotopes which describes the *rp*-process. See the main text for details. An earlier version of this reaction network has been used in the following works (Fisker 2004; Fisker et al. 2004, 2005a,b, 2006) but it now includes the hot proton-proton chains of Wiescher et al. (1989). The network is described in more detail in Fisker et al. (2006).

tervals, so their daughters are not included. The hot proton-proton chains of Wiescher et al. (1989) are also included. Above the ^{64}Ge waiting point only isotopes between the proton drip line and the boundary towards the valley of stability where half lives exceed 1 minute are included. This is sufficient because protons capture on high-Z isotopes only during the burst's peak temperature, which is only sustained for a few seconds. Weak rates up to $Z = 32$ are taken from Fuller et al. (1980, 1982a,b) and Langanke & Martínez-Pinedo (2001). Since only a small fraction of material is processed above $Z = 32$, it is a reasonable approximation to ignore neutrino losses from heavier isotopes (Schatz et al. 1999). These considerations significantly reduce the size of the network which decreases the simulation run-time.

The inner boundary, i.e. towards the neutron star crust, has been slightly improved compared to previous work which used either a massive substrate (Woosley et al. (2004)) or parameter values (Rembges (1999)). This work uses the neutron star core code of Brown (2000, 2003) which calculates the thermal luminosity emanating from the crust given the temperature at the atmosphere-ocean interface. The code includes pair, photo, and plasmon neutrino emission. The neutrino luminosity is only a few percent of the thermal luminosity but still several orders of magnitude larger than the hydrodynamical luminosity uncertainty from the conservative formulation of mechanical equations. Different types of convection occur when thermal fluctuations cause instabilities to grow. Their rate of growth determine the eddy-velocity, so all instabilities can be treated by the mixing length theory (MLT) implementation. The present work only includes the Schwarzschild-Ledoux instability, because it is the dominant form of convection during the burst (which is the only period relevant to this paper), whereas secular instabilities (e.g. semi-convection) occurring in between bursts are negligible at high accretion rates, because the diffusion speed is smaller than the advection speed of the accretion. The initial model was computed by running the simulation for hundreds of bursts until the burst ashes had advected completely to the bottom of the model and the computational envelope was in thermal balance with the neutron star core model. At this point, the envelope was considered to be self-consistent,

that is, independent of any possibly unphysical initial values, and a typical X-ray burst was picked for analysis.

3. Burst simulations

Table 2 shows a sequence of five typical bursts for comparison with observations. Out of all known sources only GS 1826-238 (see Kong et al. 2000), which is also known as "the clocked burster" (Ubertini et al. 1999), shows a sequence of nearly identical bursts owing to its very stable accretion flow (Galloway et al. 2004). It is also called "the text book burster" (Bildsten 2000), since it fits the thermonuclear flash model well (Cumming 2003).

Galloway et al. (2004) provided a detailed summary of observations of GS 1826-238 during the years 1997–98, 1997–2000, and 2002: The burst recurrence time between the years 1997 and 2000 was 4.10 ± 0.08hr while the 2002 bursts had an average recurrence time of 3.56 ± 0.03hr. This is quite close to our average of 3.77 ± 0.16hr from table 2. The accretion rate has not been accurately established due to uncertainties in distance, $d = 4$–8kpc, but our choice of accretion rate (see section 2) falls within the estimated range of Galloway et al. (2004).

The average rise time

$$\delta t^{\infty}_{\rm rise} = t^{\infty}_{L=L_{\rm peak}} - t^{\infty}_{L=0.02L_{\rm peak}} \qquad (1)$$

of our model is 9.5 ± 0.5s which is somewhat longer than the observed range of 4.75–7s. The average decay time

$$\delta t^{\infty}_{\rm decay} = t^{\infty}_{\ln(L_{peak}/L)=1} - t^{\infty}_{L=L_{\rm peak}} \qquad (2)$$

of our model is 19.9 ± 1.0 which is closer to the observed range of 14.7–19.1s. The rise time of a H/He-ignited XRB mostly depends on the ratio of H to He in the ignition region and somewhat less on the waiting points in the *rp*-process. The decay time depends on the conductivity that determines the cooling rate as well as residual nuclear burning and energy release from the β^+-decaying ashes produced by the burst. Woosley et al. (2004) showed that the decay timescale of the luminosity is sensitive to the beta decay rates. Comparing the rise and decay time scales of our model to GS 1826-238 therefore suggests that our model either accretes more hydrogen relative to helium than GS 1826-238 or that the metallicity of the accreted matter in our model ($Z = 0.019$) is lower than the metallicity of the accreted matter of GS 1826-238.

The ratio of persistent fluence, E^{∞}_p, to burst fluence, E^{∞}_b is given by

$$\alpha \equiv \frac{E^{\infty}_p}{E^{\infty}_b} = \frac{\int_t^{t+\Delta t} L^{\infty}_p dt}{\int_t^{t+\Delta t} L^{\infty}_b dt}. \qquad (3)$$

Here we find an average value of 68.6 ± 2.2. This value only includes bolometric burst energy that is thermally emitted and thus excludes neutrino emission from β^+-decays. The computed value is higher than the 41.7 ± 1.6 value of Galloway et al. (2004) but it agrees with the 60 ± 7 value of Ubertini et al. (1999).

In this paper, we analyze the first burst of table 2. Fig. 1 shows the luminosity for the analyzed burst as a function of time. When comparing it to observations, it should be kept in mind that our model assumes a spherical symmetric ignition. In reality, ignition most likely occurs at a single point on the neutron star from where the flame front spreads with a velocity of $v \sim 5 \cdot 10^5\,{\rm cm\,s^{-1}}$ via a convective deflagration front. The burning front circumnavigates the neutron star in $\tau \sim \pi R/v \sim 2$s eventually covering the entire neutron star surface (Fryxell & Woosley 1982). Therefore Fig. 1 may be thought of as the luminosity of a single point under the assumption of negligible lateral heat transport.

The luminosity is the combined product of the energy released from nuclear reactions at different depths and the energy released from the accretion impact. The Kippenhahn diagram in Fig. 2 shows the specific nuclear energy release rate as a function of column density and time as well as the extent of the convective zone. The ignition region is easily identified from the sudden and rapid increase in nuclear energy generation. This causes a temperature spike that triggers a convective instability. Since convection transports heat very efficiently, the zones above the ignition point also ignite. This is clearly seen in Fig. 2. However, this heat transport quickly restores the shallower radiative/conductive temperature gradient and convection quickly ends. The Kippenhahn diagram also demonstrates how nuclear energy generation decreases as fuel depletes and how residual helium

#	$\Delta t^{\infty}_{\rm peak-peak}$	$L^{\infty}_{\rm peak}$	$\delta t^{\infty}_{\rm rise}$	$\delta t^{\infty}_{\rm decay}$	E^{∞}_{b}	α
1	3.84hr	7.7×10^{37}ergs s^{-1}	9.2s	18.5s	3.2×10^{39}ergs	72
2	3.76	7.9	9.6	20.4	3.3	69
3	3.89	7.4	10.3	21.4	3.5	68
4	3.85	7.7	9.3	19.7	3.4	68
5	3.50	7.8	9.3	19.7	3.1	66
–	3.77 ± 0.16	7.7 ± 1.9	9.5 ± 0.5	19.9 ± 1.0	3.3 ± 0.2	68.6 ± 2.2

Table 2: The table shows calculated observables for 5 consecutive model bursts together with averages. $\Delta t^{\infty}_{\rm peak-peak}$ is the recurrence time in hours measured as the time between the respective burst and the next burst for an observer at infinity. The peak luminosity, $L^{\infty}_{\rm peak}$, is given in units of $10^{37}\,{\rm ergs}\cdot{\rm s}^{-1}$ and includes the accretion luminosity. The rise time, $\delta t^{\infty}_{\rm rise}$. The decay time, $\delta t^{\infty}_{\rm decay}$ as measured from infinity is given as the e-folding time in s of the thermal decay of the luminosity. The ratio of persistent fluence, E^{∞}_{p}, to burst fluence, E^{∞}_{b}, is given by α. See main text for details.

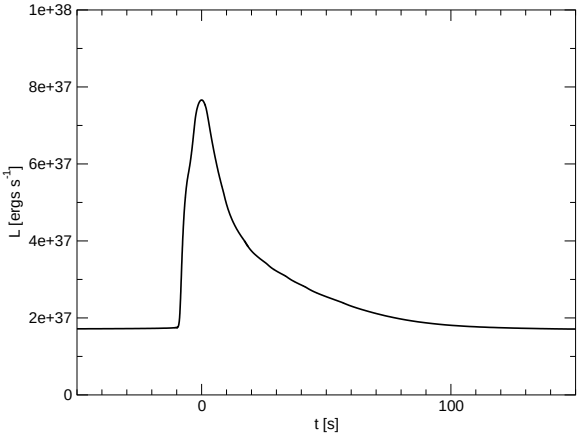

Fig. 1.— The total (redshifted) luminosity from accretion and nuclear burning as seen from an observer at infinity as a function of coordinate time for a typical burst. The timescale has been reset so that $t = 0$ corresponds to the peak luminosity of the burst. The rise time, $\delta t^{\infty}_{\rm rise} = (1+z)^{-1}\tau^{0}_{\rm rise}$, is 9.2 s. The e-folding decay time, $\tau^{\infty}_{\rm decay} == (1+z)^{-1}\tau^{0}_{\rm decay}$, is 20.4 s.

from the previous burst contributes to nuclear reactions below the ignition region. Still, most of the nuclear energy is released not at the point of ignition, but in the hydrogen rich layers just above the ignition region.

4. Reaction flow

Runaways occurring in a mixed H/He layer mainly proceed via the *rp*-process (Wallace & Woosley (1981)), where the characteristic timescale, $\tau_{rp} \sim \sum T_{1/2}$, is given by the sum of the half-lives of the β-decays in the reaction flow (van Wormer et al. (1994)). However, depending on the flow pattern, a simultaneously occurring (α, p)-process, which does not depend on β-decays, may decrease the timescale through the *sd*-shell nuclei (Wallace & Woosley (1981); Schatz et al. (1998); Fisker et al. (2004)). As the runaway lasts several seconds for a H/He-ignited XRB, the temperature gradient only produces a minor convective instability.

The analysis of a one-dimensional X-ray burst model is very complex, as the model is characterized by rapidly changing temperature conditions and nuclear reaction sequences in each layer. All these effects are tightly interconnected through energy generation and heat transport by radiation and convection. Since the different layers interact and also burn differently due to different compositions and temperatures, the burst can not be understood based on the burning of one layer only, but must be analyzed using several different burning layers. We split our analysis into four regions,

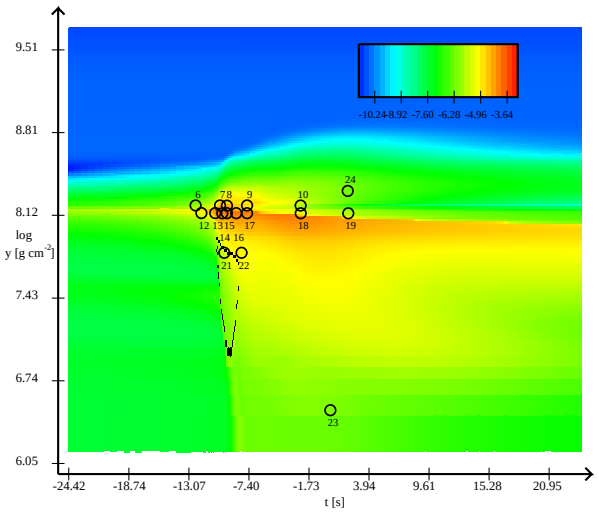

Fig. 2.— The logarithmic ($\log_{10}$) specific nuclear energy release rate in units of s^{-1} as a function of logarithmic ($\log_{10}$) relativistic column density (see footnote 2) and coordinate time as well as the extent of the convective zone (black sail shaped outline). The numbered black circles correspond to the descriptions of the reaction flow in §4 and the numbered circles in Fig. 3. Starting from the top of the figure, they are: ocean (4.5), ignition region (4.1.2–4.1.6, 4.1.1 is not shown), above ignition region (4.2.2–4.2.9), 4.2.1 and 4.2.10 are not shown), bottom of the convective region (4.3.1–4.3.2), and surface (4.4.1).

which are sufficiently different to merit separate attention: the region around the ignition point, the convective region, the surface, and the ocean. These regions are shown in Fig. 3, which shows a trace in temperature and density during the burst for different depths (pressures) for a complete revolution of the limit cycle.

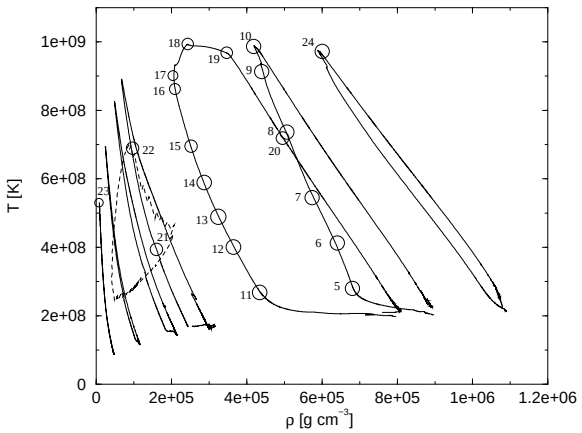

Fig. 3.— From left to right (solid line): $y = 2.1 \times 10^6 g/cm^2$ (surface), $y = 1.3 \times 10^7 g/cm^2$ (top of the convective region), $y = 3.2 \times 10^7 g/cm^2$, $y = 4.7 \times 10^7 g/cm^2$ (bottom of the convective region), $y = 1.0 \times 10^8 g/cm^2$ (above ignition), $y = 1.2 \times 10^8 g/cm^2$ (ignition point), and $y = 1.5 \times 10^8 g/cm^2$ (ocean). The dashed line indicate the region which is convective during the rising of the burst. The circles and their associated numbers correspond to the figures in §4 and the numbered circles Fig. 2.

Following the cooling of the previous burst, the individual layers reach their lowest temperature and highest density of the cycle. The subsequent accretion increases the hydrogen content of the layer, which in turn lowers the density, because the increased electron abundance of hydrogen requires less mass to maintain the hydrostatic pressure (Joss (1977); Joss & Li (1980)) compared to the heavier and more neutron-rich ashes (Hanawa & Fujimoto (1984)). This is most clearly seen in Fig. 3 just above the ignition region, which decreases its density by about a factor two during the quiescent phase, as the electron-rich surface ashes of the previous burst sink into this region. For an accretion rate of $\dot{M} = 1.12 \cdot 10^{17} g/s$ and a recurrence time of $\Delta t \approx 11000s$, the neutron star accretes a mass of $\Delta M = \dot{M} \cdot \Delta t \approx 1.1 \cdot 10^{21} g$

$(5.5 \cdot 10^{-13} M_\odot)$ in between bursts. This means that matter above $y = 5.8 \times 10^7 \mathrm{g/cm^2}$ is freshly accreted, whereas matter below that depth consists of the old surface ashes from the previous burst(s). Therefore the initial composition in the ignition region is characterized by heavier nuclei with a relatively low hydrogen and helium abundance compared to the accreted matter. When the matter ignites the rising temperature eventually reduces the degeneracy of the electrons. From this point on, the rising temperature leads to a decreases in density (see Fig. 3) until the fuel is exhausted shortly after the peak temperature is reached. The β^+-decays during and after the *rp*-process decrease the electron abundance, which increases the density as the envelope cools. The separation in density between the rising leg and the decaying leg of the temperature and density trace in Fig. 3 therefore reflects the change in composition. Clearly, the composition change is large around the ignition regions and small near the surface. The different compositions and hydrostatic pressures with corresponding temperatures and densities of the burning regions change dynamically on a nuclear timescale defined as $\min(dt/d\ln Y_i)$, where Y_i is the abundance of the ith isotope. Therefore the analysis of the nuclear reaction flow proceeds in a different way compared to previous works, which assumed solar abundances burning at fixed densities and temperatures and described the integrated flow over many minutes (van Wormer et al. (1994); Rembges et al. (1997)); instead the instant flow rate is described as the thermodynamic state variables change.

The net reaction flow rate from isotope i to isotope j is defined by

$$f_{ij} = -f_{ji} = \dot{Y}_{i\to j} - \dot{Y}_{j\to i}\,, \qquad (4)$$

where $\dot{Y}_{i\to j}$ is the time rate-of-change of the abundance of the ith isotope resulting from all reactions converting isotope i to isotope j. The flow-rates for the different points in time along the temperature and density traces in Fig. 3 will be shown in the flowcharts of the following sections for the ignition point, the region above it, the convective zone, the surface (of our model), and the ashes entering the ocean. In these figures the main reaction-flow is described by the heavy lines. Very thick lines indicate $(p,\gamma)(\gamma,p)$-equilibrium. Thin lines indicate a flow rate just above 10^{-8}mol/g/s increasing their thickness logarithmically to a maximum of 10^{-5}mol/g/s after which they stay constant. Also shown are the mass fractions, $X_A = \sum_{A_i=A} X_i$, for a given mass, A, as a function of mass number. If $X_A > 0.20$ for any A, the bar is cut off and replaced with a dotted line in which case the mass fraction can be read in the figure caption.

4.1. Ignition region

Between bursts, the surface ashes from the previous burst sink down under the weight of the newly accreted matter while the hot CNO cycle transforms hydrogen into helium. The hot CNO cycle is beta-limited and therefore burns at a fixed rate that mainly depends on the concentration of ^{14}O and ^{15}O. It is partially moderated by a quiescent breakout via the $^{15}\mathrm{O}(\alpha,\gamma)^{19}\mathrm{Ne}$ reaction which depletes ^{15}O and thus slows down the conversion of hydrogen into helium. This is discussed in more detail in Fisker et al. (2006). The reaction flow can subsequently return to the hot CNO cycle via the hot CNO bi-cycle $^{19}\mathrm{Ne}(\beta^+\nu)$ ($T_{1/2}$ = 17.22s) $^{19}\mathrm{F}(p,\alpha)$ $^{16}\mathrm{O}(p,\gamma)$ $^{17}\mathrm{F}(p,\gamma)$ $^{18}\mathrm{Ne}(\beta^+,\nu)$ ($T_{1/2} = 1.672$s) $^{18}\mathrm{F}(p,\alpha)^{15}\mathrm{O}$ which speeds up the conversion of hydrogen to helium and thus influences the composition for the runaway. This cycle is discussed in more detail in Cooper & Narayan (2006). The hot CNO cycle increases the ^{4}He concentration until a runaway of the extremely temperature sensitive triple-alpha reaction ensues and causes a spike in the nuclear energy release rate. The triple-alpha reaction creates ^{12}C, which immediately captures two protons to become ^{14}O, causing the abundance of ^{14}O ($T_{1/2} = 76.4$s) to increase, since ^{14}O ($T_{1/2} = 76.4$s) decays too slowly (see Fig. 4).

Meanwhile the increasing temperature of the nascent nuclear runaway leads to a breakout of the hot CNO cycle into the *rp*-process. The details are described in the following subsections, where we describe the reaction flow in terms of temperature, density, and proton and alpha fractions as the time develops. The time is synchronized, so $t = 0$ coincides with the peak surface luminosity.

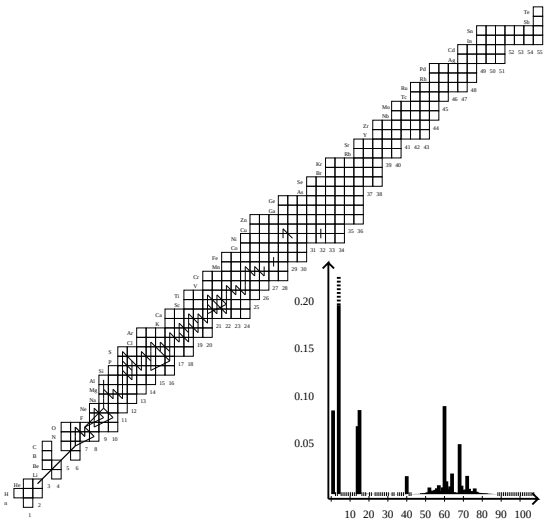

Fig. 5.— Ignition: $T = 2.86 \cdot 10^8$K, $\rho = 6.81 \cdot 10^5$g/cm^3, $X = 0.09$, $Y = 0.42$, $t = -103.078$s. (see the end of §4.0 for an explanation of the diagram).

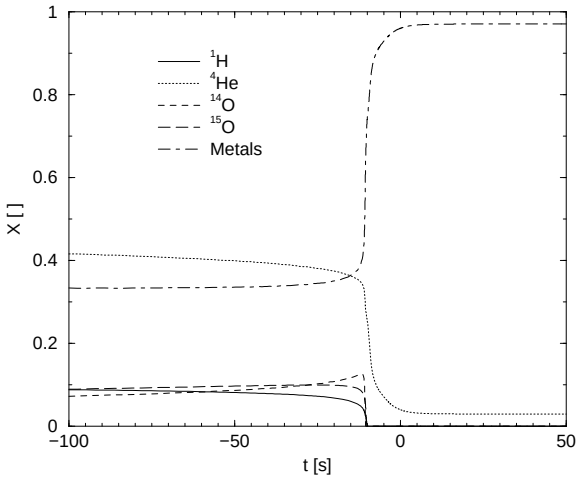

Fig. 4.— The hydrogen, helium, CNO type matter, and metal (the rest) mass fractions as a function of time. The time scale has been synchronized to coincide with the burst luminosity peak at $t = 0$. Notice the run-up in ^{14}O immediately prior to the runaway. Also note that the hydrogen in the ignition region is completely exhausted during the burst, while about $\sim 5\%$ helium remains.

4.1.1. Fig. 5: $T = 2.86 \cdot 10^8 K$, $\rho = 6.81 \cdot 10^5 g/cm^3$, $X = 0.09$, $Y = 0.42$, $t = -103.078 s$

At this time the increasing temperature has caused the flow rate of $^{15}\mathrm{O}(\alpha,\gamma)^{19}\mathrm{Ne}$ (see Fisker et al. (2006) for a detailed discussion of this rate) to reach 10% of the $^{15}\mathrm{O}(\beta^+,\nu)^{15}\mathrm{N}$ rate establishing a breakout of the hot CNO cycle (the 1% limit was breached at $t = -558$s) extending into the light iron region. At this point proton captures establish a flow out of ^{19}Ne. The matter in this flow can no longer return to the hot CNO cycle and the reaction flow proceeds with $^{19}\mathrm{Ne}(p,\gamma)$ $^{20}\mathrm{Na}(p,\gamma)$ ^{21}Mg, where it is blocked by photodisintegration, because of the $^{21}\mathrm{Mg}(p,\gamma)(\gamma,p)^{22}$Al-equilibrium. Therefore the flow proceeds via $^{21}\mathrm{Mg}(\beta^+,\nu)$ ($T_{1/2} = 0.124$s) $^{21}\mathrm{Na}(p,\gamma)$ $^{22}\mathrm{Mg}(\beta^+,\nu)$ ($T_{1/2} = 3.32$s) $^{22}\mathrm{Na}(p,\gamma)$ $^{23}\mathrm{Mg}(p,\gamma)$ $^{24}\mathrm{Al}(p,\gamma)$ ^{25}Si.

Here the flow branches into either $^{25}\mathrm{Si}(\beta^+,\nu)$ ($T_{1/2} = 0.198$s) $^{25}\mathrm{Al}(p,\gamma)$ ^{26}Si ($T_{1/2} = 1.84$s) (p,γ) ^{27}P or $^{25}\mathrm{Si}(p,\gamma)$ $^{26}\mathrm{P}(\beta^+,\nu)$ ($T_{1/2} = 0.020$s) $^{26}\mathrm{Si}(p,\gamma)$ ^{27}P or $^{25}\mathrm{Si}(p,\gamma)$ $^{26}\mathrm{P}(p,\gamma)$ $^{27}\mathrm{S}(\beta^+,\nu)$ ^{27}P all of which have ^{27}P as the end point. The characteristic time depends on the mass fraction weighed harmonic mean of the half lives of the beta decays along respective pathways. As the temperature rises, the proton capture branches become initially

more dominant but then decrease again as photodisintegration of the weakly proton bound and short lived proton-rich P and S isotopes steers the flow away from the drip line. Yet at this particular temperature the beta decay path of ^{25}Si dominates the proton capture to ^{26}P.

From this point the flow continues to ^{30}S, which has a half life of 1.07s, via ^{27}P(β^+,ν) ($T_{1/2}$ = 0.242s) ^{27}Si(p,γ) ^{28}P(p,γ) ^{29}S(β^+,ν) ($T_{1/2}$ = 0.146s) ^{29}P(p,γ). The Q-value for proton capture on ^{30}S is only 290.6keV, which leads to photodisintegration of ^{31}Cl at higher temperatures. At later times this can have a large effect on the observed luminosity of the burst (Fisker et al. 2004). At this point proton capture still dominates, so the flow proceeds via ^{30}S(p,γ) ($T_{1/2}$ = 1.07s) ^{31}Cl(β^+,ν) ($T_{1/2}$ = 0.270s) ^{31}S. ^{31}S ($T_{1/2}$ = 2.13s) either beta decays and returns the reaction flow to ^{28}Si via ^{31}P(p,α) ^{28}Si or captures a proton followed by the reaction sequence ^{31}S(p,γ) (Iliadis et al. (1999)) ^{32}Cl(β^+,ν) ($T_{1/2}$ = 0.285s) ^{32}S(p,γ) ^{33}Cl(p,γ) ^{34}Ar(β^+,ν) ($T_{1/2}$ = 0.811s) ^{34}Cl(p,γ) ^{35}Ar(p,γ) (Iliadis et al. (1999)) ^{36}K(β^+,ν) ($T_{1/2}$ = 0.302s) ^{36}Ar(p,γ) ^{37}K(p,γ) ^{38}Ca.

Since ^{39}Sc and ^{40}Sc are almost proton unbound the flow must wait for ^{38}Ca ($T_{1/2}$ = 0.416s) and ^{39}Ca ($T_{1/2}$ = 0.799s) to β^+-decay before the flow stops at the well-bound ^{40}Ca isotope. A CaScTi cycle forms at ^{40}Ca via ^{40}Ca(p,γ) ^{41}Sc(p,γ) ^{42}Ti(β^+,ν) ($T_{1/2}$ = 0.189s) ^{42}Sc(p,γ) ^{43}Ti(β^+,ν) ($T_{1/2}$ = 0.429s) ^{43}Sc(p,α) ^{40}Ca. The breakout from this cycle occurs through proton capture on ^{43}Sc, leading to a reaction flow through ^{44}Ti and ^{45}V ending at ^{52}Fe.

The total timescale for this sequence is (c.f. van Wormer et al. (1994)) $\tau = \ln(2)^{-1}\sum T_{1/2} \sim 8$s, which is slower than the time it takes to cover the star with a deflagration wave by a factor of four (Fryxell & Woosley 1982). Therefore a one-dimensional approximation is still reasonable. Later when the (α,p)-process ignites and the temperature increases, the reaction flow will move closer to the drip line decreasing the β-half-lives, thus making the timescales comparable. At that point, our model is no longer fully predictive of hydrodynamically influenced (extensive) observables such as the time-dependent luminosity. However, our model still provides a local (intensive) description of the burning conditions, and therefore a realistic description of the reaction flow.

4.1.2. Fig. 6: $T = 3.99 \cdot 10^8 K$, $\rho = 6.41 \cdot 10^5 g/cm^3$, $X = 0.05$, $Y = 0.36$, $t = -12.938s$

Approximately 90 seconds later the ^{14}O$(\alpha,p)^{17}$F reaction reaches 1/3 of the flow rate of the ^{15}O$(\alpha,\gamma)^{19}$Ne-reaction. This starts the first hot CNO bi-cycle: ^{14}O(α,p) ^{17}F(p,γ) ^{18}Ne(β^+,ν) ^{18}F$(p,\alpha)^{15}$O which runs alongside the second bi-cycle discussed above in §4.1.

At this stage ^{22}Mg$(p,\gamma)^{23}$Al and ^{22}Mg(β^+,ν) ($T_{1/2}$ = 3.34s)^{22}Na become comparable. Consequently the flow path through ^{22}Mg(p,γ) ^{23}Al(p,γ) ^{24}Si(β^+,ν) ($T_{1/2}$ = 0.190s) ^{24}Al competes with ^{22}Mg(β^+,ν) ($T_{1/2}$ = 3.34s) ^{22}Na(p,γ) ^{23}Mg(p,γ) ^{24}Al effectively creating a shortcut. Since the flow rates are about equal, the effective timescale becomes the flow rate weighted harmonic mean of the two half-lives $\approx$ 0.10s, which is much faster than before. This reduces the total timescale to reach ^{40}Ca to $\sim$ 5s. A similar shortcut exists with ^{25}Si(p,γ) ^{26}P(p,γ) ^{27}S(β^+,ν) ($T_{1/2}$ = 0.021s) ^{27}P competing with ^{25}Si(β^+,ν) ($T_{1/2}$ = 0.188s) ^{25}Al(p,γ) ^{26}Si(p,γ) ^{27}P however, here the proton capture Q-value is only 141keV, so the faster path is reduced by photodisintegration.

At this time, the concentration of ^{31}Cl has peaked and is now being destroyed by photodisintegration. Therefore the flow must pass through the ^{30}S(β^+,ν) ($T_{1/2}$ = 1.08s) reaction, which is the slowest weak reaction in the flow and adds about a second to the total timescale.

Reaching ^{31}S the flow now branches again. Instead of going through the slower ^{31}S(β^+,ν) ($T_{1/2}$ = 2.13s) ^{31}P(p,γ) ^{32}S(p,γ) ^{33}Cl, the flow can now go directly through either ^{31}S(p,γ) ^{32}Cl(β^+,ν) ($T_{1/2}$ = 0.293s) ^{32}S(p,γ) ^{33}Cl or ^{31}S(p,γ) ^{32}Cl(p,γ) ^{33}Ar(β^+,ν) ($T_{1/2}$ = 0.153s) ^{33}Cl which shaves another 2 seconds off the characteristic time for the rp-process.

The flow now breaks into the pf-shell nuclei by proton-captures on ^{39}Ca and ^{40}Ca (Wiescher & Görres (1989)). The very fast β^+-decays on the highly radioactive Sc and Ti isotopes cause the flow to spread (Fig.6) and make an analysis of the timescales difficult. The CaScTi cycle discussed in the previous section now has proton capture breakouts via ^{42}Ti(p,γ) ^{43}V, ^{43}Ti(p,γ)

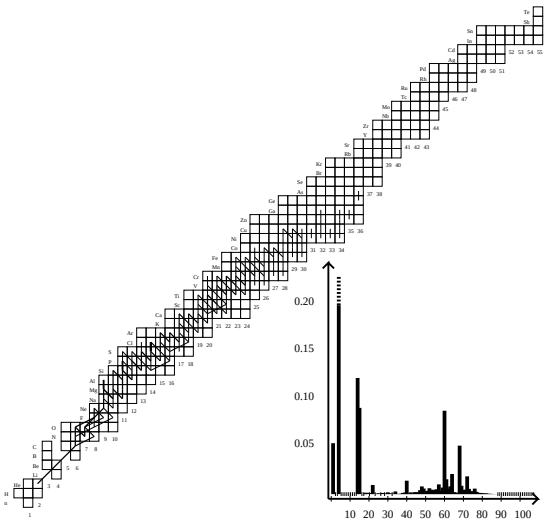

Fig. 6.— Ignition: $T = 3.99 \cdot 10^8$K, $\rho = 6.41 \cdot 10^5$g/cm^3, $X = 0.05$, $Y = 0.36$, $t = -12.938$s. (see the end of §4.0 for an explanation of the diagram).

^{44}V, and ^{43}Sc(p,γ) ^{44}Ti. The breakout reactions are followed by several combinations of proton capture and beta decays before the reaction flow passes through the ^{45}V bottleneck, either by β^+-decay ($T_{1/2} = 0.59$s) or proton capture to ^{46}Cr. The next bottleneck is ^{48}Cr which can be reached from ^{46}V by either ^{46}V(β^+,ν) ($T_{1/2} = 0.429$s) ^{46}Ti(p,γ) ^{47}Ti(p,γ) ^{48}Cr or ^{46}V(p,γ) ^{47}Cr(β^+,ν) ($T_{1/2} = 0.497$s) ^{47}V(p,γ) ^{48}Cr or ^{46}V(p,γ) ^{47}Cr(p,γ) ^{48}Mn(β^+,ν) ($T_{1/2} = 0.030$s) ^{48}Cr. The ^{48}Cr bottleneck has a half life of $T_{1/2} = 2.02$h which makes it "stable" on the timescale of the burst. The ^{48}Cr(p,γ) ^{49}Mn reaction is therefore important at this stage because it is the only way for the flow to proceed.

After capturing a proton the flow proceeds from ^{49}Mn to ^{50}Mn via either a beta decay followed by a proton capture or vice versa. The flow from ^{50}Mn to ^{51}Mn proceeds in a similar manner. ^{51}Mn has a half life of $T_{1/2} = 35.3$m so ^{51}Mn captures a proton and becomes ^{52}Fe. There is a small reaction flow from ^{52}Fe to ^{56}Fe via a series of proton captures followed by beta decays. ^{56}Fe then captures several protons to ^{59}Cu, before alternating proton captures and beta decays finally lead to ^{60}Ni. There are also proton captures on Ni-Zn ashes from the previous burst at this time.

4.1.3. Fig. 7: $T = 5.37 \cdot 10^8 K$, $\rho = 5.81 \cdot 10^5 g/cm^3$, $X = 0.03$, $Y = 0.31$, $t = -10.631s$

At this point the ^{14}O(α,p) ^{17}F reaction is 5 times stronger than the ^{15}O$(\alpha,\gamma)^{19}$Ne reaction. This starts the (α,p)-process (Wallace & Woosley (1981); Schatz et al. (1998); Fisker et al. (2004)) which here runs as ^{14}O(α,p) ^{17}F(p,γ) ^{18}Ne(α,p) ^{21}Na(p,γ) ^{22}Mg(α,p) ^{25}Al(p,γ) ^{26}Si. Another (α,p)-reaction that now becomes important is ^{21}Mg(α,p) ^{24}Al. This reaction soon overpowers the ^{22}Al β^+-decay out of the ^{21}Mg$(p,\gamma)(\gamma,p)$ ^{22}Al equilibrium, which becomes largely irrelevant for the burst.

While ^{30}S, ^{31}Cl and ^{32}Ar are in $(p,\gamma)(\gamma,p)$-equilibrium, the main flow has to proceed through the beta decay of ^{30}S. This has a significant impact on the energy generation as it causes a considerable delay in the *rp*-process.

In the Ca-Fe region, the flow moves closer to the drip line with ^{43}V(p,γ) ^{44}Cr(β^+,ν) ($T_{1/2} = 0.030$s) ^{44}V and ^{47}Mn(p,γ) ^{48}Fe(β^+,ν) ($T_{1/2} = 0.030$s) ^{48}Mn becoming more active. Above Fe, the flow extends to ^{60}Zn as more proton rich nuclei start to capture protons. With ^{60}Zn's $T_{1/2} = 4.10$m half life, ^{59}Cu's $T_{1/2} = 83.1$s half life, and the stable ^{58}Ni, the ^{60}Zn(p,γ) ^{61}Ga reaction is the only way to move the flow forward. In addition,

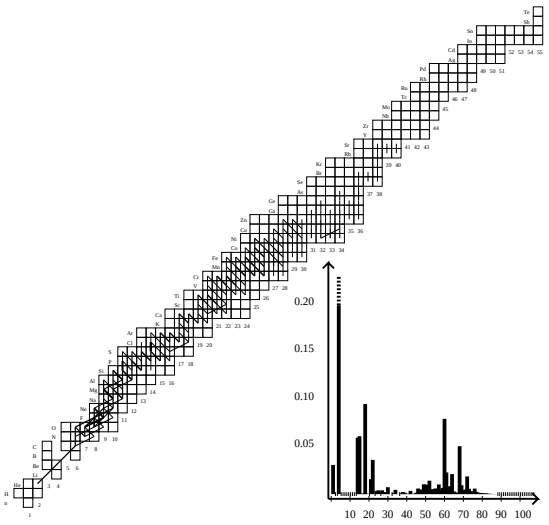

Fig. 7.— Ignition: $T = 5.37 \cdot 10^8$K, $\rho = 5.81 \cdot 10^5$g/cm^3, $X = 0.03$, $Y = 0.31$, $t = -10.631$s. (see the end of §4.0 for an explanation of the diagram).

proton captures on heavier isotopes produced by the previous burst move the composition towards the drip line. This compositional inertia effect increases the average mass and charge of the final ashes.

4.1.4. Fig. 8: $T = 7.30 \cdot 10^8 K$, $\rho = 5.07 \cdot 10^5 g/cm^3$, $X = 3.5 \times 10^{-4}$, $Y = 0.26$, $t = -9.980s$

The protons are now almost exhausted. This can also be seen in Fig. 4. At this point the proton-rich isotopes near the drip lines decay towards the valley of stability, where they undergo (α, p)-reactions. As Fig. 8 shows, with less than 1% hydrogen remaining proton captures are still occurring although they are weakening. In addition, hydrogen from (α, p)-reactions can still serve as a catalyst in the (α, p)-process.

The (α, p)-process now extends further and includes the ^{25}Si(α, p) ^{28}P and ^{26}Si(α, p) ^{29}P reactions. SiPS, PSCl, ArKCa, and CaScTi cycles are observed with ^{28}Si, ^{32}P, ^{36}Ar and ^{40}Ca as the nexus, but they are not consequential to the flow. In the Zn region, the flow proceeds through the ^{59}Cu(β^+, ν) $(T_{1/2} = 84.5$s) decay, which is stronger than the ^{60}Zn (p, γ) ^{61}Ga reaction. The reaction flow stops at ^{63}Ge and the ^{64}Ge waiting point. This coincides with the depletion of the protons, so even as ^{64}Ge subsequently decays there is no further flow into heavier isotopes.

4.1.5. Fig. 9: $T = 9.03 \cdot 10^8 K$, $\rho = 4.46 \cdot 10^5 g/cm^3$, $X = 3.3 \times 10^{-6}$, $Y = 0.12$, $t = -8.075s$

At this point the region receives more heat from adjacent regions than it produces. This allows endothermic (α, p)-reactions on more bound nuclei to occur. The significant amounts of ^{60}Zn produced by the *rp*-process are now decaying. A weak *rp*-process from light to heavy isotopes is still occurring, driven by the small amounts of protons released by (α, p)-reactions in the $A = 20$–36 region. Therefore the general lack of protons ensures that the *rp*-process at this point does not proceed beyond $A = 64$. Additionally the shortage of protons means that the flow moves away from the proton drip line with the remaining protons generally capturing on the currently most abundant nuclei (now determined by half-life) with the largest cross sections and the lowest Coulomb barriers, that is, nuclei in the $A = 20$–36 range.

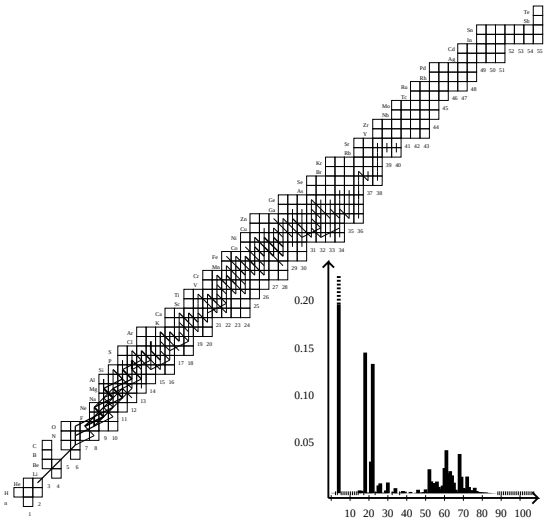

Fig. 8.— Ignition: $T = 7.30 \cdot 10^8$K, $\rho = 5.07 \cdot 10^5$g/cm^3, $X = 3.5 \times 10^{-4}$, $Y = 0.26$, $t = -9.980$s. (see the end of §4.0 for an explanation of the diagram).

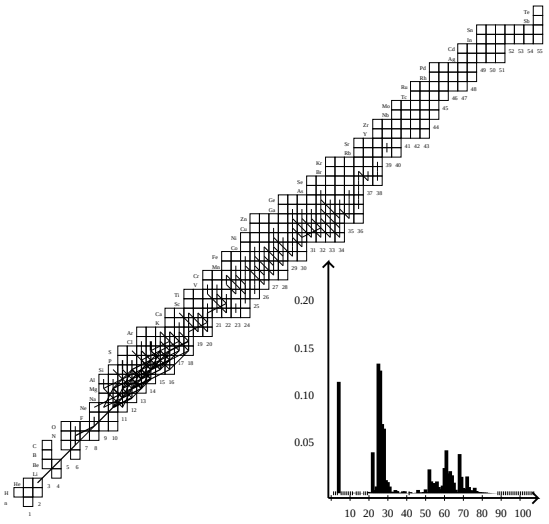

Fig. 9.— Ignition: $T = 9.03 \cdot 10^8$K, $\rho = 4.46 \cdot 10^5$g/cm^3, $X3.3 \times 10^{-6}$, $Y = 0.12$, $t = -8.075$s. (see the end of §4.0 for an explanation of the diagram).

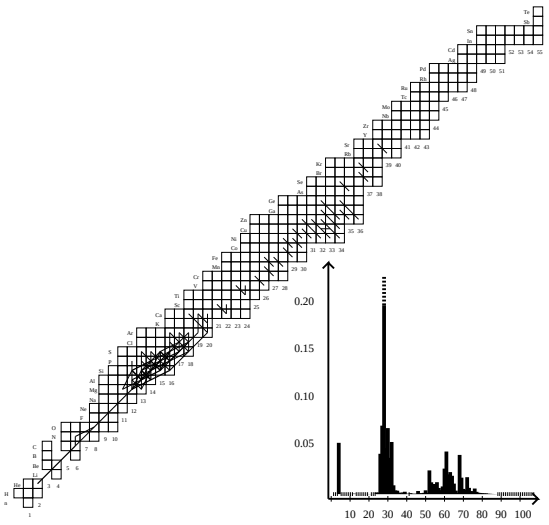

Fig. 10.— Ignition: $T = 9.89 \cdot 10^8$K, $\rho = 4.20 \cdot 10^5$g/cm^3, $X = 2.4 \times 10^{-9}$, $Y = 0.05$, $X_{28} = 0.22$, $t = -3.018$s. (see the end of §4.0 for an explanation of the diagram).

4.1.6. Fig. 10: $T = 9.89 \cdot 10^8 K$, $\rho = 4.20 \cdot 10^5 g/cm^3$, $X = 2.4 \times 10^{-9}$, $Y = 0.05$, $X_{28} = 0.22$, $t = -3.018s$

The flow through the alpha-chain nuclei is clearly seen in Fig. 10, which shows the reaction flow at maximum temperature. We note that ^{12}C(p,γ) ^{13}N(α,p) ^{16}O is much stronger than the direct ^{12}C(α,γ) ^{16}O-reaction as long as (α,p)-reactions are still possible on heavier isotopes (Weinberg et al. 2006). The reaction flow continues with (α,γ)-reactions up to ^{36}Ar. Eventually the downward heat flux from the upper regions becomes too weak to sustain the (α,p)-reactions and the reactions die out leaving only radioactive isotopes, which slowly decay to more stable ones.

4.2. Above the ignition region

It is relevant to know the reaction flow and its energy release at the depth that reaches the highest temperature during the burst, because this layer heats up adjacent, colder regions. The highest temperature of a burst ignited by mixed hydrogen and helium is reached just above the point of point of ignition.

4.2.1. Fig. 11: $T = 2.80 \cdot 10^8 K$, $\rho = 4.29 \cdot 10^5 g/cm^3$, $X = 0.41$, $Y = 0.43$, $t = -103.078s$

The ^{15}O$(\alpha,\gamma)^{19}$Ne-reaction is less important at this depth, because less "hot CNO material" has been created by the triple-alpha process due to lower temperatures and densities. So while the reaction burns off the existing ^{15}O, the runaway at this depth occurs when the heat from the ignition point below increases the 3α reaction rate. Once the runaway is triggered the reaction flow through the CNO region is eventually dominated by ^{12}C(p,γ) ^{13}N(p,γ) ^{14}O(α,p) ^{17}F bypassing ^{15}O$(\alpha,\gamma)^{19}$Ne. This is because ^{14}O ($T_{1/2} = 70.6$s) does not have the time to decay during the runaway. However, the ^{15}O$(\alpha,\gamma)^{19}$Ne-reaction does establish a very weak flow to the iron-region along a flow path identical to the initial path in the deeper region. Although this region contains former surface ashes no further captures occur at this point.

4.2.2. Fig. 12: $T = 3.97 \cdot 10^8 K$, $\rho = 3.68 \cdot 10^5 g/cm^3$, $X = 0.400$, $Y = 0.406$, $t = -12.387s$

At this point the ^{14}O$(\alpha,p)^{17}$F reaction reaches 1/3 of the flow rate of the ^{15}O$(\alpha,\gamma)^{19}$Ne-reaction establishing the first hot CNO bi-cycle (discussed

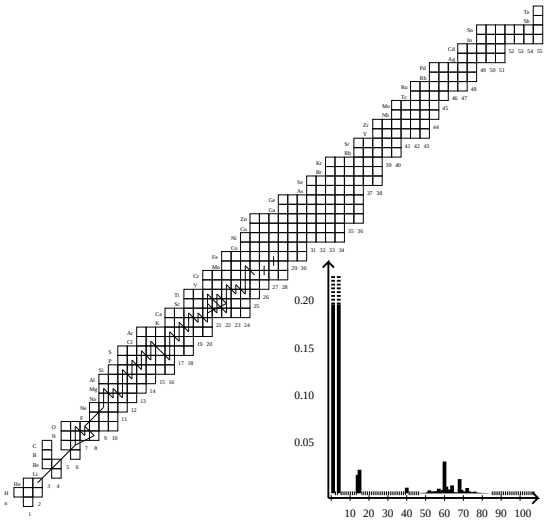

Fig. 11.— Above ignition: $T = 2.80 \cdot 10^8$K, $\rho = 4.29 \cdot 10^5$g/cm^3, $X = 0.41$, $Y = 0.43$, $t = -103.078$s. (see the end of §4.0 for an explanation of the diagram).

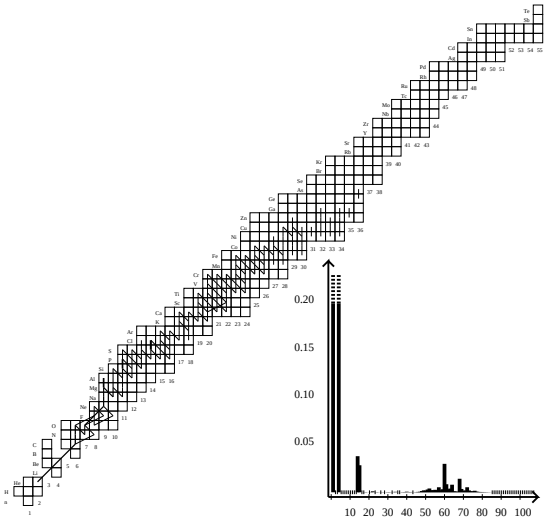

Fig. 12.— Above ignition: $T = 3.97 \cdot 10^8$K, $\rho = 3.68 \cdot 10^5$g/cm^3, $X = 0.400$, $Y = 0.406$, $t = -12.387$s. (see the end of §4.0 for an explanation of the diagram).

in §4.1.2). This occurs at a lower temperature compared to the deeper ignition region because of the higher $^{14}O/^{15}O$ abundance ratio. In contrast to the ignition point, the second bi-cycle (discussed in §4.1) is not established, because temperature and hydrogen abundance are high enough to destroy ^{19}Ne immediately by proton capture.

The rapidly increasing heat flux from the ignition point below enables short cuts such as $^{22}Mg(p,\gamma)$ $^{23}Al(p,\gamma)$ $^{24}Si(\beta^+,\nu)$ ($T_{1/2} = 0.190$s) ^{24}Al to dominate over $^{22}Mg(\beta^+,\nu)$ ($T_{1/2} = 3.37$s) $^{22}Na(p,\gamma)$ $^{23}Mg(p,\gamma)$ ^{24}Al. From this point on the reactions are identical to the flow described in §4.1.2. Since there is more hydrogen in this region the reaction on isotopes heaver than Mn are faster, yet since the temperature at this point in time (same as §4.1.2) is lower, the the capture rates on lighter isotopes than Mn are slower.

4.2.3. Fig. 13: $T = 4.44 \cdot 10^8 K$, $\rho = 3.46 \cdot 10^5 g/cm^3$, $X = 0.398$, $Y = 0.402$, $t = -11.091s$

$^{14}O(\alpha,p)^{17}F$ is now as strong as $^{15}O(\alpha,\gamma)^{19}Ne$. The flow through the $^{31}Cl(\beta^+,\nu)$ ($T_{1/2} = 0.270$s) waiting point is approximately equal to the flow through the ^{30}S ($T_{1/2} = 1.08$s) waiting point, but the latter will quickly become dominant as rising temperatures prevent the formation of ^{31}Cl due to photodisintegration.

In the Zn region, the flow stops at the long lived ^{59}Cu ($T_{1/2} = 84.7$s) and ^{60}Zn ($T_{1/2} = 4.29$m), but the temperature is not yet sufficiently high for proton captures to established a reaction flow to heaver nuclei, nor has sufficient time passed to allow a substantial amount of material to decay through these two nuclei. It is interesting to note that processing to heaver material either depends on the temperature becoming sufficiently high for the $^{60}Zn(p,\gamma)(\gamma,p)$ ^{61}Ga equilibrium to allow (p,γ)-reactions on ^{61}Ga or the temperature remaining sufficiently low for the flow to proceed through the faster $^{59}Cu(\beta^+,\nu)$ ^{59}Ni-reaction.

4.2.4. Fig. 14: $T = 5.75 \cdot 10^8 K$, $\rho = 2.19 \cdot 10^5 g/cm^3$, $X = 0.393$, $Y = 0.387$, $t = -10.418s$

At this point the $^{18}Ne(\alpha,p)$ ^{21}Na-reaction acts as a breakout reaction into the *rp*-process via $^{12}C(p,\gamma)$ $^{13}N(p,\gamma)$ $^{14}O(\alpha,p)$ $^{17}F(p,\gamma)$ $^{18}Ne(\alpha,p)$ ^{21}Na and so forth instead of waiting for the $T_{1/2} = 1.67$s beta-decay of ^{18}Ne. The $^{18}Ne(\alpha,p)$ ^{21}Na-reaction is thus especially important as most of the energy release in the atmosphere originates from the *rp*-process at lower depths and higher hydrogen concentrations (see Fig. 2). However, presently 90% of the the flow through the lighter isotopes stops at the ^{30}S ($T_{1/2} = 1.09$s) waiting point with only a small flux continuing through its decay. This causes a temporary dip in the energy production, though the higher temperature ensures a flow close to the drip line from Ca to Ni. This flow is, however, slowed down at the $N = 28$ isotones due to the long half-lives of ^{55}Co ($T_{1/2} = 10.3$h) and ^{56}Ni ($T_{1/2} = 24.9$h), which effectively prevent any beta decays of these isotopes. It is also interesting to note the (p,α)-reactions on the heavier Cu isotopes that return the reaction flow back to Ni while releasing helium.

At this point there is a weak flow out of ^{59}Cu which allows additional proton captures via $^{59}Ni(p,\gamma)^{60}Cu(p,\gamma)$ $^{61}Zn(p,\gamma)$ ^{62}Ga which can either decay or capture an additional proton to ^{63}Ge which then decays. If ^{62}Ga decays it captures two additional protons and becomes ^{64}Ge. It is also possible to reach ^{65}Ge through the decay of ^{63}Ga and subsequent proton captures and beta decays. Heavier isotopes are generated through proton captures on ashes from the previous burst. None of these are beta decaying though.

4.2.5. Fig. 15: $T = 6.97 \cdot 10^8 K$, $\rho = 2.51 \cdot 10^5 g/cm^3$, $X = 0.381$, $Y = 0.372$, $t = -9.994s$

A couple of seconds after it begins to dominate the reaction flow breakout via $^{14}O(\alpha,p)$ ^{17}F becomes so fast that any ^{14}O is immediately destroyed. Consequently ^{15}O is only created via the first hot CNO bi-cycle. However, the bi-cycle will become void, because it is now sufficiently hot for alpha-particles to penetrate the Coulomb barrier of ^{18}Ne, thus skipping its $T_{1/2} = 1.67$s β^+-decay.

Additional (α,p)-reactions now occur on ^{21}Mg and ^{25}Si. The latter circumvents the ($T_{1/2} = 0.176$s) half-life of ^{25}Si, thus shortening the characteristic reaction flow timescale in the $A = 20$–30 region. The timescale is dominated by the $^{30}S(\beta^+,\nu)$ ($T_{1/2} = 1.09$s) ^{30}P reaction, which carries 98% of the flow. $^{24}Si(\alpha,p)$ ^{27}P is not as significant since ^{24}Si is destroyed by photodisintegra-

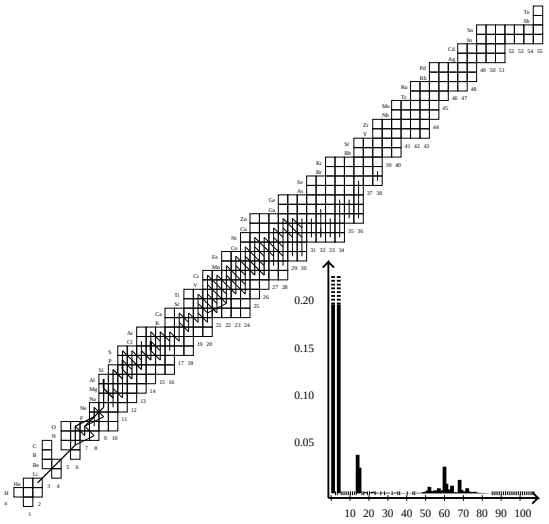

Fig. 13.— Above ignition: $T = 4.44 \cdot 10^8$K, $\rho = 3.46 \cdot 10^5$g/cm^3, $X = 0.398$, $Y = 0.402$, $t = -11.091$s. (see the end of §4.0 for an explanation of the diagram).

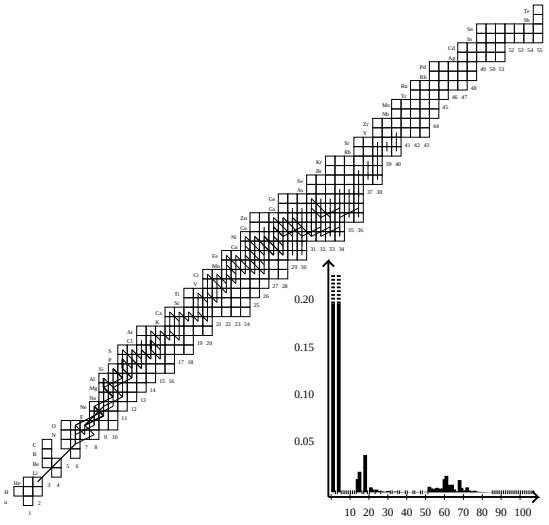

Fig. 14.— Above ignition: $T = 5.75 \cdot 10^8$K, $\rho = 2.19 \cdot 10^5$g/cm^3, $X = 0.393$, $Y = 0.387$, $t = -10.418$s. (see the end of §4.0 for an explanation of the diagram).

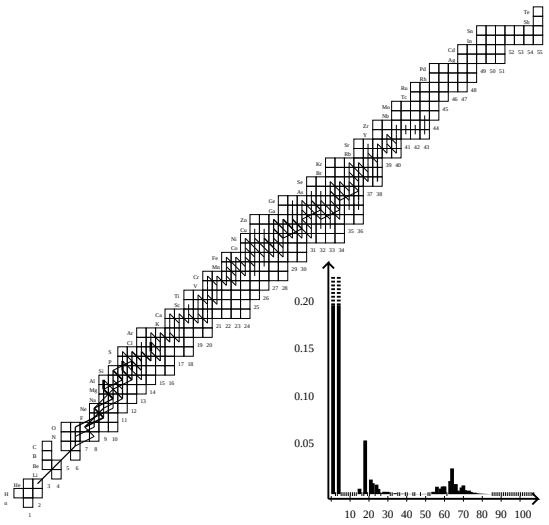

Fig. 15.— Above ignition: $T = 6.97 \cdot 10^8$K, $\rho = 2.51 \cdot 10^5$g/cm^3, $X = 0.381$, $Y = 0.372$, $t = -9.994$s. (see the end of §4.0 for an explanation of the diagram).

tion. It is interesting to note a weak but present ^{18}Ne(α,γ) ^{22}Mg, which competes with the (α,p)-process.

The flow up to ^{58}Ni remains the same. The increased temperature and flow sets up NiCuZn, ZnGaGe and GeAsSe cycles on ^{58}Ni, ^{60}Zn, and ^{66}Ge. We note that there is still no flow out of ^{64}Ge(p,γ) ^{65}As as ^{65}As is weakly proton bound and 2p capture (Schatz et al. 1998) is not effective. Therefore the reaction flow proceeds via the slow beta decay ^{64}Ge(β^+,ν) ($T_{1/2} = 84.9$s) ^{64}Ga or the lighter ^{63}Ga(β^+,ν) ($T_{1/2} = 26.6$s) ^{63}Zn.

At $N = 33$ the flow reaches ^{67}Se ($T_{1/2} = 0.060$s) and ^{68}Se ($T_{1/2} = 35.5$s). Further progress either depends on another 2p-reaction (Schatz et al. 1998) or ^{68}Se or ^{67}As decaying. A similar challenge is posed by ^{72}Kr ($T_{1/2} = 17.2$s), ^{76}Sr ($T_{1/2} = 8.9$s) and ^{80}Zr ($T_{1/2} = 3.9$s). Presently the flow does not continue to heavier isotopes, though some proton captures begin on heavier isotopes present in ashes of the previous burst.

4.2.6. Fig. 16: $T = 8.34 \cdot 10^8 K$, $\rho = 2.15 \cdot 10^5 g/cm^3$, $X = 0.358$, $Y = 0.346$, $t = -9.097s$

At this time the temperature is sufficiently high for photodisintegration of ^{27}S to prevent the shortcut, which was previously established between ^{25}Si and ^{27}P. However, at the same temperature the ^{21}Mg(α,p) ^{24}Al and the ^{22}Mg(α,p) ^{25}Al reactions become significant. In addition, ^{24}Si(α,p) ^{27}P, ^{25}Si(α,p) ^{28}P, and ^{26}Si(α,p) ^{29}P become significant. Circumventing ^{30}S(β^+,ν) ($T_{1/2} = 1.09$s) ^{30}P becomes possible through the ^{29}S(α,p) ^{32}Cl-reaction which at this point is not as strong as the beta decay.

^{38}Ca enters $(p,\gamma)(\gamma,p)$-equilibrium with ^{39}Sc, but since ^{39}Sc is proton unbound, the flow must await the ($T_{1/2} = 0.04$s)-decay of ^{38}Ca which becomes a bottleneck. Heavier isotopes with $N > 32$ up to ^{84}Mo ($T_{1/2} = 3.6$s) are produced now. Some hydrogen is capturing on $N = 43$ and $N = 44$ isotones in the ashes from the previous burst.

4.2.7. Fig. 17: $T = 8.96 \cdot 10^8 K$, $\rho = 2.07 \cdot 10^5 g/cm^3$, $X = 0.327$, $Y = 0.326$, $t = -8.075s$

At this time the ^{28}S(α,p) ^{31}Cl, ^{29}S(α,p) ^{32}Cl, and ^{30}S(α,p) ^{33}Cl are all active. The latter now competes directly with the ^{30}S beta decay. This competition is especially important at lower accretion rates (Fisker et al. 2004). The *rp*-process reaches now ^{88}Ru ($T_{1/2} = 1.1$s). There are no significant proton captures on heavier isotopes.

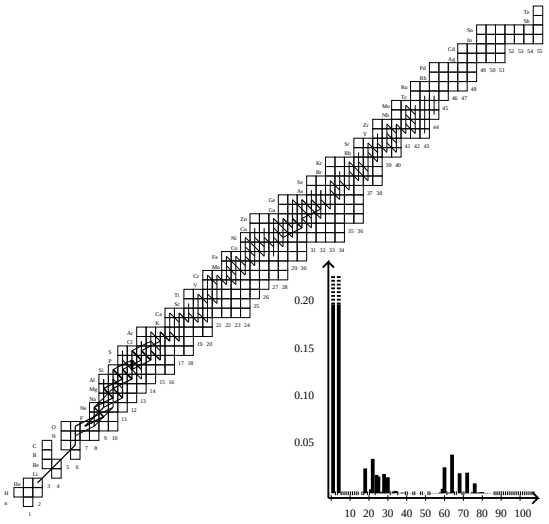

Fig. 16.— Above ignition: $T = 8.34 \cdot 10^8$K, $\rho = 2.15 \cdot 10^5$g/cm^3, $X = 0.358$, $Y = 0.346$, $t = -9.097$s. (see the end of §4.0 for an explanation of the diagram).

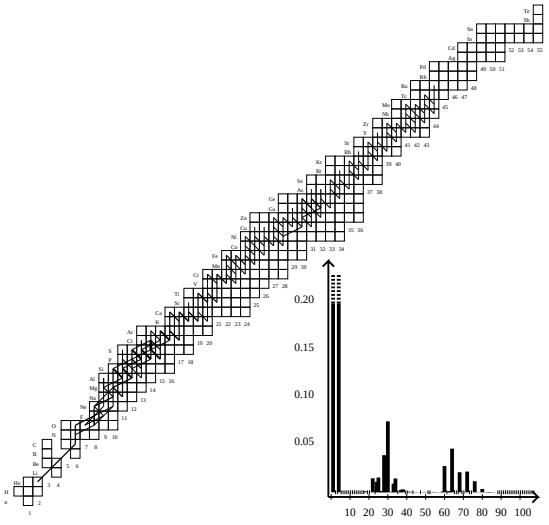

Fig. 17.— Above ignition: $T = 8.96 \cdot 10^8$K, $\rho = 2.07 \cdot 10^5$g/cm^3, $X = 0.327$, $Y = 0.326$, $t = -8.075$s. (see the end of §4.0 for an explanation of the diagram).

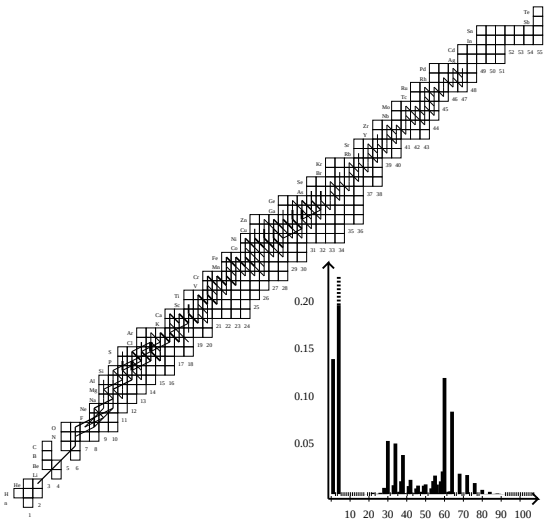

Fig. 18.— Above ignition: $T = 9.93 \cdot 10^8$K, $\rho = 2.43 \cdot 10^5$g/cm^3, $X = 0.143$, $Y = 0.234$, $t = -3.013$s. (see the end of §4.0 for an explanation of the diagram).

4.2.8. Fig. 18: $T = 9.93 \cdot 10^8 K$, $\rho = 2.43 \cdot 10^5 g/cm^3$, $X = 0.143$, $Y = 0.234$, $t = -3.013s$

This region has now reached its maximum temperature. The reaction flow-path is very similar to the flow in Fig. 17. One notable difference is the ^{34}Ar(α, p) ^{37}K reaction which is the last among the (α, p)-reactions for the temperatures encountered in type I XRBs. Additionally, the *rp*-process now continues to ^{92}Pd and ^{93}Pd. This effectively constitutes the end of the *rp*-process which is short of the prediction of Schatz et al. (2001a). The reason is the thermal and compositional inertia as well as the much lower peak temperature achieved by our model. If these are ignored, the flow does reach the SnSbTe cycle as shown by Woosley et al. (2004). This flow structure is maintained until hydrogen runs out.

4.2.9. Fig. 19: $T = 9.62 \cdot 10^8 K$, $\rho = 3.54 \cdot 10^5 g/cm^3$, $X = 2.5 \times 10^{-5}$, $Y = 0.175$, $X_{60} = 0.346$, $t = 1.476s$

The last protons capture on the currently most abundant nuclei, namely the isotopes in the Ca-Ge region, while the main reaction flow is characterized by beta decays towards the valley of stability along constant mass numbers. With helium still burning, the (α, p)-process up to $A = 36$ is still active. However, the ^{12}C(p, γ) ^{13}N(α, p) ^{16}O path prevents the formation of ^{17}F. This means that the (α, p)-process starts on ^{21}Na, which is reached via ^{16}O(α, γ) ^{20}Ne(p, γ) ^{21}Na.

4.2.10. Fig. 20: $T = 6.97 \cdot 10^8 K$, $\rho = 5.10 \cdot 10^5 g/cm^3$, $X = 1.0 \times 10^{-11}$, $Y = 0.089$, $X_{60} = 0.347$, $t = 28.788s$

Half a minute after the burst peak the *rp*-process no longer operates and the temperature has decreased by 30%. From here on, most of the ^{12}C produced so far will be eliminated via ^{12}C(p, γ) ^{13}N(α, p) ^{16}O followed by (α, γ)-reactions up to ^{32}S. Meanwhile, heavier isotopes decay until they reach the valley of stability.

4.3. Convective region

The size of the convective region is shown in Fig. 3, which shows a trace of the burst conditions for different depths (pressures) during a complete revolution of the limit cycle. Note that the convective zone only exist during the phase where the temperature rises (the cycle revolves clockwise). The figure shows that the convective zone does not reach the top of our model for this burst, but stays in a narrow region between $y = 1.3 \times 10^7$g/cm^2 and $y = 4.7 \times 10^7$g/cm^2. Additionally, this burst does not reach super-Eddington luminosities, so

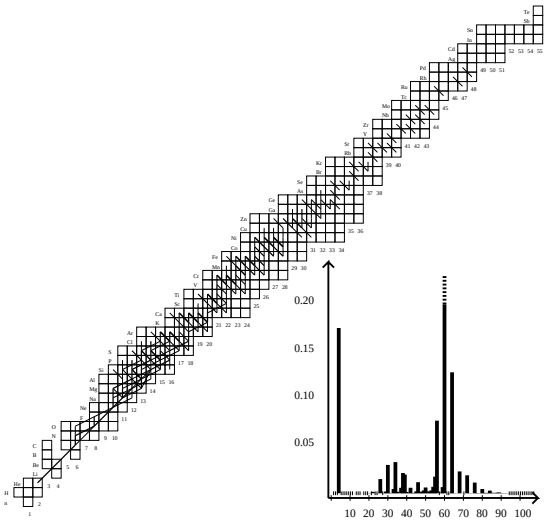

Fig. 19.— Above ignition: $T = 9.62 \cdot 10^8$K, $\rho = 3.54 \cdot 10^5$g/cm^3, $X = 2.5 \times 10^{-5}$, $Y = 0.175$, $X_{60} = 0.346$, $t = 1.476$s. (see the end of §4.0 for an explanation of the diagram).

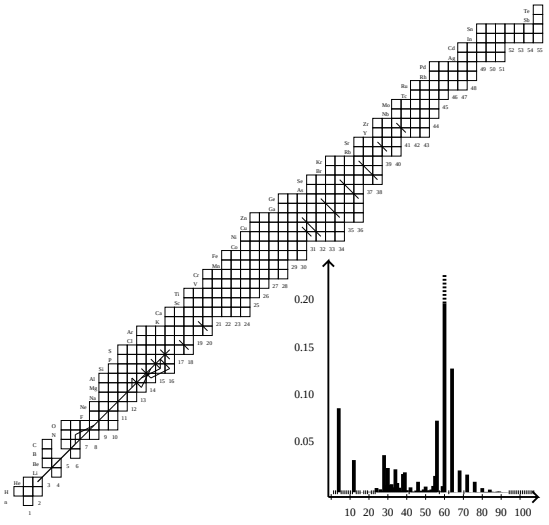

Fig. 20.— Above ignition: $T = 6.97 \cdot 10^8$K, $\rho = 5.10 \cdot 10^5$g/cm^3, $X = 1.0 \times 10^{-11}$, $Y = 0.089$, $X_{60} = 0.347$, $t = 28.788$s. (see the end of §4.0 for an explanation of the diagram).

no ashes will be ejected by a radiatively driven wind, something that is possible in helium-ignited bursts (Weinberg et al. 2006).

The quantitative analysis of the turbulent convective burning is complicated by the mixing of matter between convective zones, which occurs as soon and as long as a slightly superadiabatic temperature gradient is established. However, the convective timescale, $\tau_{con.} \equiv \Lambda / v_{edd.} \sim 10^{-6}$–$10^{-5}$s $\ll \tau_{rp}$, is generally faster than the typical timescale of the *rp*-process, so the explosive burning will have almost the same composition throughout the entire convective zone (see the convective model of Rembges (1999) which assumes identical composition throughout the convective zone for comparison) although burning happens at different temperatures and densities at the top and bottom of the convective zone respectively. Furthermore, turbulent convective burning does not happen above temperatures of 7×10^8 K, so the (α, p)-process, which has a much shorter timescale, does not become active. Therefore this region could be computed by models with a simplified description of the compositional evolution but a more complex (2D) hydrodynamical implementation. The following analysis of this region concentrates on the bottom of the convective region, where it is hotter and denser and where therefore the reactions proceed faster.

4.3.1. Fig. 21: $T = 3.92 \cdot 10^8 K$, $\rho = 1.161 \cdot 10^4 g/cm^3$, $X = 0.610$, $Y = 0.363$, $t = -10.229 s$

The convective period during this burst lasts about 2.2 s during which fresh unburned matter from the colder top of the convective zone mixes into the warmer bottom and back again. This means that temperature dependent particle-captures are effectively weaker, whereas the weak decays remain unaltered. Due to this short duration, the convective region attains a maximum temperature of only $\sim 0.7 \cdot 10^9$KK ($\sim 0.9 \cdot 10^9$K is the peak temperature reached at this depth later once convection has ceased). This is not sufficient to induce the short cuts in the reaction flow such as (α, p)-reactions or the upper leg of *rp*-process bifurcations available to the deeper layers and described in the previous sections; instead the initial reaction flow is mostly represented by the flow chart of Fig. 21.

At this point, the first hot CNO bi-cycle, $^{14}\mathrm{O}(\alpha, p)$ $^{17}\mathrm{F}(p, \gamma)$ $^{18}\mathrm{Ne}(\beta^+, \nu)$ ($T_{1/2} = 1.67$s) $^{18}\mathrm{F}(p, \alpha)^{15}\mathrm{O}$ already dominates the second hot CNO bi-cycle, $^{19}\mathrm{Ne}(\beta^+, \nu)$ ($T_{1/2} = 17.2$s) $^{19}\mathrm{F}(p, \alpha)$ $^{16}\mathrm{O}(p, \gamma)$ $^{17}\mathrm{F}(p, \gamma)$ $^{18}\mathrm{Ne}(\beta^+, \nu)$ ($T_{1/2} = 1.67$s) $^{18}\mathrm{F}(p, \alpha)^{15}\mathrm{O}$, as the temperature is high enough for the $^{19}\mathrm{Ne}(p, \gamma)$ ^{20}Na-reaction to dominate the slow $^{19}\mathrm{Ne}(\beta^+, \nu)$ ($T_{1/2} = 17.2$s) ^{19}F. From this point ^{20}Na captures another proton so $^{20}\mathrm{Na}(p, \gamma)$ $^{21}\mathrm{Mg}(\beta^+, \nu)$ ($T_{1/2} = 0.124$s) $^{21}\mathrm{Na}(p, \gamma)$ ^{22}Mg.

Here the flow bifurcates to either $^{22}\mathrm{Mg}(\beta^+, \nu)$ ($T_{1/2} = 3.46$s) $^{22}\mathrm{Na}(p, \gamma)$ $^{23}\mathrm{Mg}(p, \gamma)$ ^{24}Al or $^{22}\mathrm{Mg}(p, \gamma)$ $^{23}\mathrm{Al}(p, \gamma)$ $^{24}\mathrm{Si}(\beta^+, \nu)$ ($T_{1/2} = 0.191$s) ^{24}Al. A similar bifurcation exists at $^{25}\mathrm{Si}(p, \gamma)$ $^{26}\mathrm{P}(p, \gamma)$ $^{27}\mathrm{S}(\beta^+, \nu)$ ($T_{1/2} = 0.021$s) ^{27}P competing with $^{25}\mathrm{Si}(\beta^+, \nu)$ ($T_{1/2} = 0.189$s) $^{25}\mathrm{Al}(p, \gamma)$ $^{26}\mathrm{Si}(p, \gamma)$ ^{27}P.

The ^{30}S waiting point still acts as a bottleneck with a small leak via $^{30}\mathrm{S}(p, \gamma)$ $^{31}\mathrm{Cl}(\beta^+, \nu)$ ($T_{1/2} = 0.272$s) ^{31}S. However, this leak is quickly reduced by photodisintegration. The flow passes then through the $^{34}\mathrm{Ar}(\beta^+, \nu)$ ($T_{1/2} = 0.824$s) bottleneck and on through $^{37}\mathrm{Ca}(\beta^+, \nu)$ ($T_{1/2} = 0.155$s) $^{37}\mathrm{K}(p, \gamma)$ $^{38}\mathrm{Ca}(\beta^+, \nu)$ ($T_{1/2} = 0.423$s) $^{38}\mathrm{K}(p, \gamma)$ $^{39}\mathrm{Ca}(\beta^+, \nu)$ ($T_{1/2} = 0.808$s) $^{39}\mathrm{K}(p, \gamma)$ ^{40}Ca into the *pf*-shell isotopes. It is interesting that the *rp*-process is already active in the ^{40}Ca–^{52}Fe region. This is because double-magic ^{40}Ca has been produced before as it represents the natural end-point of the reaction chain occurring just prior to burst ignition.

4.3.2. Fig. 22: $T = 6.90 \cdot 10^8 K$, $\rho = 9.35 \cdot 10^4 g/cm^3$, $X = 0.646$, $Y = 0.328$, $t = -8.600 s$

Fig. 22 shows the reaction flow at the maximum temperature reached during the convective phase. This temperature peak coincides with the maximum temperature in the ignition region below that drives the superadiabatic temperature gradient responsible for the convective turnover. Higher temperatures are reached at this depth once convection has stopped.

At the end of the convective phase, the (α, p)-process at the bottom of the convective region extends to ^{26}Si. Following that, the flow to heaver isotopes is impacted by the ^{30}S ($T_{1/2} = 1.10$s) waiting point. This is significant because the entire convective phase only lasts two half lives

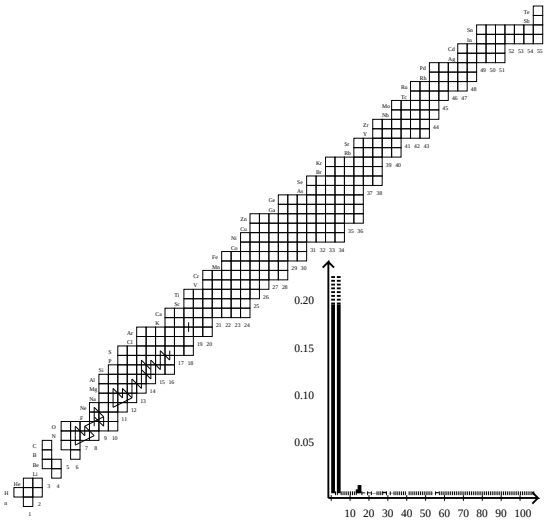

Fig. 21.— Convection region: $T = 3.92 \cdot 10^8$K, $\rho = 1.161 \cdot 10^4$g/cm^3, $X = 0.610$, $Y = 0.363$, $t = -10.229$s. (see the end of §4.0 for an explanation of the diagram).

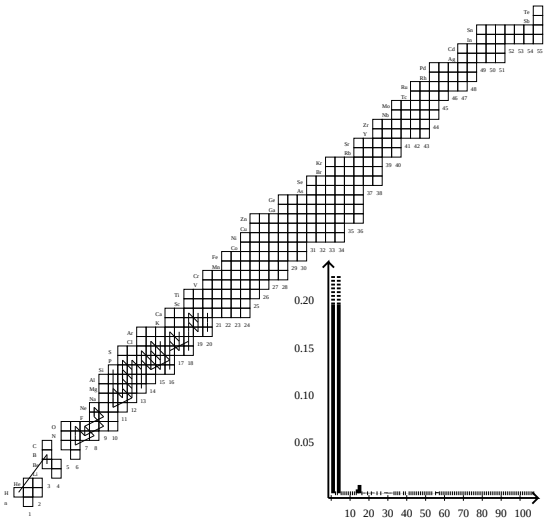

Fig. 22.— Convection region: $T = 6.90 \cdot 10^8$K, $\rho = 9.35 \cdot 10^4$g/cm^3, $X = 0.646$, $Y = 0.328$, $t = -8.600$s. (see the end of §4.0 for an explanation of the diagram).

of ^{30}S. Similarly, there are bottlenecks at ^{59}Cu ($T_{1/2}$ = 91.9s) and ^{60}Zn ($T_{1/2}$ = 5.28m) which require a ^{60}Zn(p,γ) ^{61}Ga breakout that does not happen at these temperatures during the short convection phase.

4.4. Surface region

In H/He-ignited XRBs the convective region does not extend to the top of our model. This means that if the convective model does not severely underestimate the convective strength then heavier ashes are not brought to the surface. Since the matter at the top of our model is extremely opaque with mean free photon paths of $\sim 10^{-4}$cm, the photons are in local thermal equilibrium (LTE) and exhibit a black body spectrum with no lines. Comparison between the results of this section and observations therefore require this model to be coupled with a radiative transport code (see Weinberg et al. (2006)).

4.4.1. Fig. 23: $T = 5.31 \cdot 10^8 K$, $\rho = 8.75 \cdot 10^3 g/cm^3$, $X = 0.697$, $Y = 0.281$, $t = -0.209s$

The extent of the reaction flow at the maximum temperature is shown in Fig. 23 and ends at ^{56}Ni. This region is limited by $T < 5.3 \cdot 10^8$K and the initial reactions are characterized by proton captures on the accreted heavy elements, which may have been destroyed by the surface impact (Bildsten et al. 1992).

4.5. Ocean (ashes)

The inner parts of the neutron star act as a buffer absorbing heat from the burst. However, for the accretion rate considered here the heat is radiated outwards again after the burst. Therefore the bursts do not heat the crust (Fujimoto et al. (1984)).

The early reaction flow, which is caused by conductive heating in a hydrogen depleted environment is similar to the reaction flow in Fig. 10. Later it is characterized by residual helium, which has been advected down from the previous burst, capturing on alpha-chain nuclei extending to ^{36}Ar as shown in Fig. 24. Note that ^{12}C(p,γ) ^{13}N(α,p) ^{16}O is much stronger than the direct ^{12}C(α,γ) ^{16}O-reaction. Here the protons are supplied by many weak (α,p)-reactions on stable isotopes resulting from long lived β^+-decays in the sulfur region in matter that has advected downwards from above.

5. Conclusion

Important in all the regions are the hot-CNO (bi-)cycles and their respective breakout reactions, the (α,p)-process, as well as $(p,\gamma)(\gamma,p)$-equilibria and waiting points of the *rp*-process. These are now discussed.

5.1. Hot CNO cycles

There are essentially three hot CNO cycles, specifically, the hot CNO cycle: ^{12}C(p,γ) ^{13}N(p,γ) ^{14}O(β^+,ν) ^{14}N(p,γ) ^{15}O(β^+,ν) ^{15}N(p,α) ^{12}C, the first hot CNO bi-cycle: ^{14}O(α,p) ^{17}F(p,γ) ^{18}Ne(β^+,ν) ^{18}F$(p,\alpha)^{15}$O and second hot CNO bi-cycle ^{15}O(α,γ) ^{19}Ne(β^+,ν) ^{19}F(p,α) ^{16}O(p,γ) ^{17}F(p,γ) ^{18}Ne(β^+,ν) ^{18}F$(p,\alpha)^{15}$O.

In order to activate the first hot CNO bi-cycle, via ^{14}O(α,p) ^{17}F and its breakout via ^{17}F(p,γ) ^{18}Ne(α,p) ^{21}Na, the second hot CNO bi-cycle must activate hundreds of second prior to the runaway and achieve a breakout via ^{19}Ne(p,γ) ^{20}Na. If the ^{15}O(α,γ) ^{19}Ne-reaction is too weak, the second cycle never activates which means that the first cycle does not activate either and the thermonuclear runaway does not happen (Fisker et al. 2006). These rates are therefore quite significant in connecting the hot CNO cycle to the *rp*-process. Additionally, the reaction flow, in particular the second hot CNO bi-cycle of Cooper & Narayan (2006), prior to the runaway is important for the ignition composition as it influences the concentration of hydrogen and helium which is important to the thermonuclear instability.

5.2. The (α,p)-process

The (α,p)-process is important because it is a temperature dependent process unlike the *rp*-process that contains temperature-independent β^+-decays. The (α,p)-process therefore influences the characteristic timescale of the reaction flow up to $A = 36$ after which the Coulomb barrier becomes prohibitive. Furthermore, as shown in Fisker et al. (2004), the (α,p)-reactions in the (α,p)-process lie on waiting points with ^{30}S being

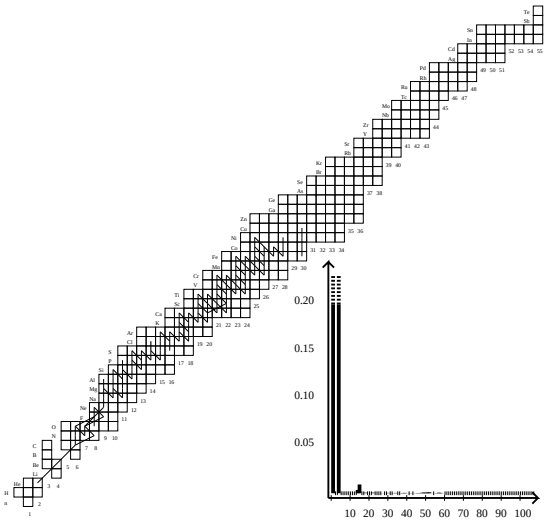

Fig. 23.— Surface: $T = 5.31 \cdot 10^8$K, $\rho = 8.75 \cdot 10^3$g/cm^3, $X = 0.697$, $Y = 0.281$, $t = -0.209$s. (see the end of §4.0 for an explanation of the diagram).

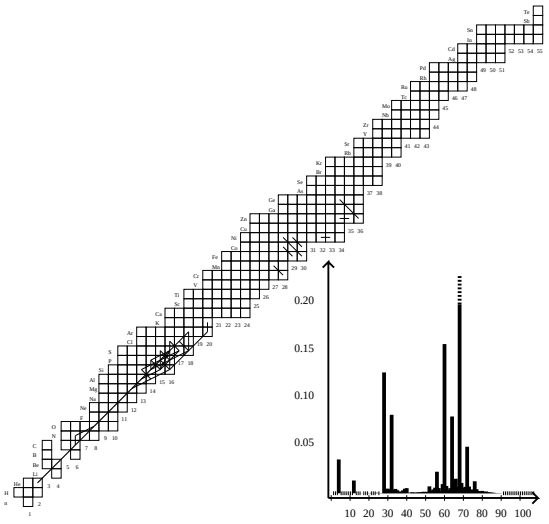

Fig. 24.— Ocean: $T = 9.55 \cdot 10^8$K, $\rho = 6.06 \cdot 10^5$g/cm^3, $X = 5.3 \cdot 10^{-11}$, $Y = 0.036$, $X_{68} = 0.22$, $t = -0.209$s. (see the end of §4.0 for an explanation of the diagram).

the most significant one. Other potential waiting points are ^{34}Ar and ^{26}Si.

The most important (α, p)-reactions for the XRB are therefore ^{26}Si(α, p) ^{29}P, ^{30}S(α, p) ^{33}Cl, and ^{34}Ar(α, p) ^{37}K. The ^{22}Mg(α, p) ^{25}Al-reaction is most likely not as important, since the flow moves through the ^{22}Mg waiting point via ^{22}Mg(p, γ) ^{23}Al before the (α, p)-reaction becomes active.

Other (α, p)-reactions are less dominant since they operate at higher temperatures and on more proton-rich nuclei which are more susceptible to photodisintegration viz. ^{21}Mg(α, p) ^{24}Al, ^{24}Si(α, p) ^{27}P, ^{25}Si(α, p) ^{28}P, ^{28}S(α, p) ^{31}Cl, and ^{29}S(α, p) ^{32}Cl. Another important (α, p)-reaction is ^{13}N(α, p) ^{16}O. The reason is that the ^{12}C(p, γ) ^{13}N(α, p) ^{16}O reaction path is stronger than the ^{12}C(α, γ) ^{16}O reaction and also stronger than the ^{13}N(p, γ) ^{14}O reaction if hydrogen is depleted (also see Weinberg et al. (2006)).

5.3. The *rp*-process

The *rp*-process evolution depends on the concentration of hydrogen and the peak temperature. The peak temperature is easily estimated as $P = a_{rad}T^4$ which assumes that the pressure is fully supported by radiation and that the dynamical pressure is negligible. This is a good assumption as the gravitational binding energy is a factor $\sim$ 20–50 higher than nuclear energy release of the burst. This dependence means that if the pressure of the ignition point is inaccurately determined, the peak temperature may be off by 10% or more which will significantly change the conclusions about the flow. Thermal and compositional inertia must be taken into account when considering the reaction flow. This was first shown by Woosley et al. (2004) who started with a pure ^{56}Fe atmosphere which allowed accreted matter to reach deeper layers. As a result Woosley et al. (2004) obtained the same results as the one-zone model of Schatz et al. (2001a) who based their ignition pressure and composition on analytical estimates. On the other hand, selfconsistently obtained bursts by Woosley et al. (2004) match the results obtained by other selfconsistent models (Rembges 1999; Fisker et al. 2003, 2004, 2005a,b) as well as this paper.

5.3.1. rp-process waiting points

Waiting points are isotopes from which further net reaction flows are (possibly temporarily) restricted due to either insufficiently high temperatures, insufficient capture particles, or the immediate photodisintegration due to a $(p, \gamma)(\gamma, p)$-equilibrium. Waiting points are easily identified by their temporary abundance spikes. If a substantial, say 20% or more, part of the flow is backed up at a given isotope for a time comparable to the time scale of the XRB, it can significantly influence the shape of the observed luminosity curve (see Fisker et al. (2004)).

During the early build up to the XRB and during the early phases of the ^{21}Mg$(p, \gamma)(\gamma, p)^{22}$Al-equilibrium, which depends on the Q-value of the proton capture reaction, ^{21}Mg must β^+-decay. The half life is short compared to the build-up phase which is on the order of hundreds of seconds. It is however comparable with the runaway time of the XRB. Therefore, the runaway depends on the ^{21}Mg(α, p) ^{24}Al reaction. Similar waiting points can be found along the (α, p)-process reaction path. They are ^{22}Mg, ^{26}Si, ^{30}S, ^{34}Ar, and ^{38}Ca. The dominant waiting point in this sequence depends on the extent of the (α, p)-process which depends on the peak temperature. If the peak temperature is extremely high e.g. $T_{peak} > 1.3 \times 10^9$K these waiting points are bypassed by the (α, p)-process. For lower peak temperatures, these waiting point along with their associated Q-values and proton capture rates become important. However, our model has never reached peak temperatures above $\sim 1.3 \times 10^9$K for accretion rates greater than $\dot{M} = 5 \cdot 10^{16}\,\mathrm{g\,s^{-1}}$ while accreting a solar composition (Anders & Grevesse 1989) on a self-consistently attained atmosphere. The ^{38}Ca waiting point might be circumvented by ^{38}Ca(p, γ) ^{39}Sc(p, γ) ^{40}Ti or ^{38}Ca$(2p, \gamma)$ ^{40}Ti.

Hot CNO-like cycles exist on well-bound isotopes such as ^{40}Ca. This isotope is particularly interesting since the flow passes through it during the quiescent phase. The low-temperature ^{43}Sc(p, γ) ^{44}Ti-reaction is therefore an important bottleneck as it determines the developing composition during the quiescent phase and thus the ignition conditions. The next bottleneck in the quiescent flow is ^{48}Cr(p, γ) ^{49}Mn. During the burst (above $T \sim 5 \cdot 10^8$K) the flow through the Ca-Ni

region goes through many β^+-decays and (p,γ)-reactions leaving no single determining reaction.

The Ni-Se region includes several waiting points. The first waiting points are ^{59}Cu and ^{60}Zn. Their half lives are of the order of the burst decay timescale and must be surpassed by proton captures in order for heavier isotopes to be produced. ^{60}Zn is in $(p,\gamma)(\gamma,p)$-equilibrium and further processing depends on the Q-value of ^{60}Zn(p,γ) ^{61}Ga. There is a possible flow via ^{61}Ga(p,γ) ^{62}Ge. A similar situation exists at ^{64}Ge. Here ^{65}As is proton-unbound, so further flow depends on either a $2p$-capture (Schatz et al. 1998) or a slow β^+-decay. This is the reason why most of the flow stops at the $A = 64$. The atmosphere cools before a substantial amount of matter can decay and be processed to heavier isotopes. Similar situations exist at ^{68}Se, ^{72}Kr, ^{76}Sr, and ^{80}Zr where the corresponding ^{69}Br, ^{73}Rb, ^{77}Y, and ^{81}Nb isotopes are also proton-unbound. These waiting points have also been identified by Schatz et al. (1998) and by Woosley et al. (2004), who showed the significance of these decays by varying groups of electron capture and β^+-decay rates up and down by 1 order of magnitude thus testing the impact of the efficiency of the reaction flow progression through the waiting points on the burst light curve.

5.4. Superbursts and convection

We showed that the peak burst temperature is less than $\sim$ 1.3GK and thus not as high as previously assumed for nuclear reaction studies. As seen in Fig. 24, this means that most of the reaction flow stops on the even-even nuclei in the $A \sim 60$ range and that Te is not created in large quantities corroborating previous multi-zone simulations of Fisker et al. (2003, 2005b); Woosley et al. (2004). At the same time carbon in the burst ashes is slowly turned into even-even nuclei in the $A \sim 28$–36 range by subsequent helium captures below the ignition zone and at the top of the ocean. This corroborates the findings of Woosley et al. (2004) and it does not favor the parameter space requirements of current superburst theories (Cumming & Bildsten 2001). However, our model did not consider sedimentation effects which may change this conclusion (Peng et al. 2007).

We find that the convective region does not reach the top of our model for mixed hydrogen/helium (sub-Eddington) bursters. Therefore we predict that any spectral lines observed during such bursts are not from material that was burned at any significant depth. However, at lower accretion rates, the convective region does reach the top of our model for helium bursters (see Fisker et al. (2005a)).

5.5. Summary

The main result of our calculations is the identification of the nuclear reaction sequences that power type I X-ray bursts. In particular, we describe the complete nuclear reaction flow as a function of time and depth, including branchings and waiting points, as it evolves with realistic, rapidly changing temperatures and densities. Clearly, the reaction sequences are more complex than previously assumed based on the analysis of much simpler models. Our work is a necessary first step towards identifying the critical nuclear reaction rates in X-ray bursts that have the largest impact on observables such as light curves, or, indirectly, the composition of the ashes. One can then also begin to disentangle the effects of nuclear burning on the luminosity (Fisker et al. 2004) from geometric effects such as the propagation of the burning front around the neutron star (Spitkovsky et al. 2002) to better explain the many different and somewhat inconsistent shapes of the observed burst luminosity profiles.

JLF and HS were supported by NSF-PFC grant PHY02–16783 through the Joint Institute of Nuclear Astrophysics[3]. FKT and JLF acknowledge support from the Swiss NSF grant 20–068031.02.

REFERENCES

Amthor, M., Galaviz, D., Heger, A., Sahkaruk, A., Schatz, H., & Smith, K. 2006, Proceedings of Science, NIC-IX, 68

Anders, E. & Grevesse, M. 1989, Geochim. Cosmochim. Acta, 53, 197

Ayasli, S. & Joss, P. C. 1982, Astrophys. J., 256, 637

[3]see http://www.JINAweb.org

Bildsten, L. 1998, in The Many Faces of Neutron Stars, ed. R. Buccheri, J. van Paradijs, & M. A. Alpar (Kluwer), 419

Bildsten, L. 2000, in Cosmic Explosions, ed. S. S. Holt & W. W. Zhang (AIP), 359

Bildsten, L., Salpeter, E. E., & Wasserman, I. 1992, Astrophys. J., 384, 143

Brown, E. F. 2000, Astrophys. J., 531, 988

—. 2003, Core code, private communication

—. 2004, Astrophys. J. Lett., 614, 57

Champagne, A. E. & Wiescher, M. 1992, Ann. Rev. Nucl. Part. Sci., 42, 39

Cooper, R. L. & Narayan, R. 2006, Astrophys. J. Lett., 648, L123

Cumming, A. 2003, Thermonuclear X-ray bursts: Theory vs. Observations, astro-ph/0309626

Cumming, A. & Bildsten, L. 2001, Astrophys. J. Lett., 559, L127

Fisker, J. L. 2004, PhD thesis, Univ. Basel

Fisker, J. L., Brown, E., Liebendörfer, M., Schatz, H., & Thielemann, F.-K. 2005a, Nucl. Phys., A758, 447

Fisker, J. L., Brown, E., Liebendörfer, M., Thielemann, F.-K., & Wiescher, M. 2005b, Nucl. Phys., A752, 604

Fisker, J. L., Görres, J., Wiescher, M., & Davids, B. 2006, Astrophys. J., 650, 332

Fisker, J. L., Hix, W. R., Liebendörfer, M., & Thielemann, F.-K. 2003, Nucl. Phys., A718, 614

Fisker, J. L., Thielemann, F.-K., & Wiescher, M. 2004, Astrophys. J. Lett., 608, L61

Fryxell, B. A. & Woosley, S. E. 1982, Astrophys. J., 261, 332

Fujimoto, M. Y., Hanawa, T., & Miyaji, S. 1981, Astrophys. J., 246, 267

—. 1984, Astrophys. J., 278, 813

Fujimoto, M. Y., Sztajno, M., Lewin, W. H. G., & van Paradijs, J. 1987, Astrophys. J., 319, 902

Fuller, G. M., Fowler, W. A., & Newman, M. J. 1980, Astrophys. J. Suppl., 42, 447

—. 1982a, Astrophys. J., 252, 715

—. 1982b, Astrophys. J. Suppl., 48, 279

Galloway, D. K., Cumming, A., Kuulkers, E., Bildsten, L., Chakrabarty, D., & Rotschild, R. E. 2004, Astrophys. J., 601, 466

Hanawa, T. & Fujimoto, M. Y. 1984, Publ. Astron. Soc. Japan, 36, 199

Hanawa, T., Sugimoto, D., & aki Hashimoto, M. 1983, Publ. Astron. Soc. Japan, 35, 491

Hansen, C. J. & van Horn, H. M. 1975, Astrophys. J., 195, 735

Herndl, H., Jörres, Wiescher, M., Brown, B. A., & van Wormer, L. 1995, Phys. Rev., C52, 1078

Hix, W. R. & Thielemann, F.-K. 1999, J. Comput. Appl. Math., 109, 321

Iliadis, C., Endt, P. M., Prantzos, N., & Thompson, W. J. 1999, Astrophys. J., 524, 434

Joss, P. C. 1977, Nature, 270, 310

—. 1978, Astrophys. J. Lett., 225, L123

Joss, P. C. & Li, F. K. 1980, Astrophys. J., 238, 287

Käppeler, F., Thielemann, F.-K., & Wiescher, M. 1998, Ann. Rev. Nucl. Part. Sci., 48, 175

Koike, O., Hashimoto, M., Arai, K., & Wanajo, S. 1999, Astron. Astrophys., 342, 464

Kong, A. K. H., Homer, L., Kuulkers, E., Charles, P. A., & Smale, A. P. 2000, Mon. Not. R. Astron. Soc., 311, 405

Langanke, K. & Martínez-Pinedo, G. 2001, Nucl. Phys., A673, 481

Liebendörfer, M., Rosswog, S., & Thielemann, F.-K. 2002, Astrophys. J. Suppl., 141, 229

Peng, F., Brown, E. F., & Truran, J. W. 2007, Astrophys. J., 654, 1022

Rembges, F. 1999, PhD thesis, University of Basel

Rembges, F., Freiburghaus, C., Rauscher, T., Thielemann, F.-K., Schatz, H., & Wiescher, M. 1997, Astrophys. J., 484, 412

Roberts, L., Hix, W., Smith, M., & Fisker, J. 2006, Proceedings of Science, NIC-IX, 202

Sakharuk, A., Elliot, T., Fisker, J. L., Hemingray, S., Kruizenga, A., Rauscher, T., Schatz, H., Smith, K., Thielemann, F.-K., & Wiescher, M. 2006, in Capture Gamma-Ray Spectroscopy and Related Topics, ed. A. Woehr & A. Aprahamian

Schatz, H. 2002, Acta. Phys. Pol. B, 33, 227

Schatz, H., Aprahamian, A., Barnard, V., Bildsten, L., Cumming, A., Ouellette, M., Rauscher, T., Thielemann, F.-K., & Wiescher, M. 2001a, Phys. Rev. Lett., 86, 3471

—. 2001b, Nucl. Phys., A688, 150

Schatz, H., Aprahamian, A., Görres, J., Wiescher, M., Rauscher, T., Rembges, J. F., Thielemann, F.-K., Pfeiffer, B., Möller, P., Kratz, K. L., Herndl, H., Brown, B. A., & Rebel, H. 1998, Phys. Rev., 294, 167

Schatz, H., Bildsten, L., Cumming, A., & Wiescher, M. 1999, Astrophys. J., 524, 1014

Schatz, H. & Rehm, K. E. 2006, Nucl. Phys., A777, 601

Spitkovsky, A., Levin, Y., & Ushomirsky, G. 2002, Astrophys. J., 566, 1018

Strohmayer, T. E. & Bildsten, L. 2006, in Compact Stellar X-ray Sources, ed. W. H. G. Lewin & M. van der Klis (Cambridge University Press)

Taam, R. E. 1980, Astrophys. J., 241, 358

—. 1993, Astrophys. J., 413, 324

Taam, R. E. & Picklum, R. E. 1979, Astrophys. J., 233, 327

Thorne, K. S. 1977, Astrophys. J., 212, 825

Ubertini, P., Bazzano, A., Cocchi, M., Natalucci, L., Heise, J., Muller, J. M., & In't Zand, J. J. M. 1999, Astrophys. J. Lett., 514, L27

van Wormer, L., Görres, J., Illiadis, C., Wiescher, M., & Thielemann, F.-K. 1994, Astrophys. J., 423, 326

Wallace, R. K. & Woosley, S. E. 1981, Astrophys. J. Suppl., 45, 389

Wallace, R. K., Woosley, S. E., & Weaver, T. A. 1982, Astrophys. J., 258, 696

Weinberg, N., Bildsten, L., & Schatz, H. 2006, Astrophys. J., 639, 1018

Weiss, A., Hillebrandt, W., Thomas, H.-C., & Ritter, H. 2004, Cox & Giuli's Principles of Stellar Structure (Cambridge, UK: Cambridge Scientific Publishers)

Wiescher, M. 2001, Nucl. Phys., A688, 241

Wiescher, M. & Görres, J. 1989, Astrophys. J., 346, 1041

Wiescher, M., Görres, J., Graff, S., Buchmann, L., & Thielemann, F.-K. 1989, Astrophys. J., 343, 352

Wiescher, M. & Schatz, H. 2001, Nucl. Phys., A693, 269

Woosley, S. E., Heger, A., Cumming, A., Hoffman, R. D., Pruet, J., Rauscher, T., Fisker, J. L., Schatz, H., Brown, B. A., & Wiescher, M. 2004, Astrophys. J. Suppl., 151, 75

Woosley, S. E. & Taam, R. E. 1976, Nature, 263, 101

This work was performed under the auspices of the U.S. Department of Energy by University of California, Lawrence Livermore National Laboratory under Contract W-7405-Eng-48.

This 2-column preprint was prepared with the AAS LaTeX macros v5.2.